1 # Lower Crustal Heterogeneity and Fractional Crystallisation Control
2 # Evolution of Small Volume Magma Batches at Ocean Island
3 # Volcanoes (Ascension Island, South Atlantic)

4
5
6
7
8
9 **K. J. CHAMBERLAIN[1, 2*], J. BARCLAY[3], K. J. PREECE,[4], R. J. BROWN[1], J. P. DAVIDSON[1]**

10
11
12
13
14
15
16
17
18
19 [1] DEPARTMENT OF EARTH SCIENCES, DURHAM UNIVERSITY, DURHAM, DH1 3LE, UK
20 [2] SCHOOL OF ENVIRONMENTAL SCIENCES, UNIVERSITY OF DERBY, DERBY, DE22 1GB, UK
21 [3] SCHOOL OF ENVIRONMENTAL SCIENCES, UNIVERSITY OF EAST ANGLIA, NORWICH, NR4 7TJ, UK
22 [4] DEPARTMENT OF GEOGRAPHY, COLLEGE OF SCIENCE, SWANSEA UNIVERSITY, SINGLETON PARK,
23 SWANSEA, SA2 8PP, UK

24
25
26
27
28
29
30
36
37
38 *Corresponding author. Phone (+44-1332-592971)
39 Email address: k.chamberlain@derby.ac.uk
40

ABSTRACT

Ocean island volcanoes erupt a wide range of magmatic compositions via a diverse range of eruptive styles. Understanding where and how these melts evolve is thus an essential component in the anticipation of future volcanic activity. Here we examine the role of crustal structure and magmatic flux in controlling the location, evolution and ultimately composition of melts at Ascension Island. Ascension Island, in the south Atlantic, is an ocean island volcano which has produced a continuum of eruptive compositions from basalt to rhyolite in its 1-million-year subaerial eruptive history. Volcanic rocks broadly follow a silica-undersaturated subalkaline evolutionary trend and new data presented here show a continuous compositional trend from basalt through trachyte to rhyolite. Detailed petrographic observations are combined with *in-situ* geochemical analyses of crystals and glass, and new whole rock major and trace element data from mafic and felsic pyroclastic and effusive deposits that span the entire range in eruptive ages and compositions found on Ascension Island. These data show that extensive fractional crystallisation is the main driver for the production of felsic melt for Ascension Island; a volcano built on thin, young, oceanic crust. Strong spatial variations in the compositions of erupted magmas reveals the role of a heterogeneous lower crust: differing degrees of interaction with a zone of plutonic rocks are responsible for the range in mafic lava composition, and for the formation of the central and eastern felsic complexes. A central core of nested small-scale plutonic, or mush-like, bodies inhibits the ascent of mafic magmas, allowing sequential fractional crystallisation within the lower crust, and generating felsic magmas in the core of the island. There is no evidence for magma mixing preserved in any of the studied eruptions, suggesting that magma storage regions are transient, and material is not recycled between eruptions.

INTRODUCTION

66   Ocean island volcanoes remain enigmatic in terms of their origin (Niu et al., 2011), evolution

67   and ability to produce a range of magmatic compositions and eruptive activity. Many ocean

68   islands such as Iceland, Socorro, and the archipelagos of Hawaii, the Galapagos and the

69   Canaries have been studied in detail (e.g. Sparks & Sigurdsson, 1987; Geist et al., 1988;

70   Ablay et al., 1998; Geist et al., 1995; Bohrson et al., 1996; Harpp & White, 2001; Koppers &

71   Staudigel, 2005; Carracedo et al., 2007; Carley et al., 2011; Mancini et al., 2015), but some

72   ocean island volcanoes remain relatively poorly understood (e.g. the Azores, St Helena), and

73   yet still pose a significant hazard to populations often living proximal to volcanic vents.

74   Ascension Island, in the south Atlantic, is an example of the latter. It is small (subaerial

75   dimensions of 8 km by 12 km), has no associated hotspot trace (cf. Hawaii, the Canaries; e.g.

76   Zhao, 2004; Montelli et al., 2004) and has erupted magmas with a wide range of

77   compositions (Daly, 1925; Coombs, 1963; Weaver et al., 1996; Kar et al., 1998; Jicha et al.,

78   2013). This compositional diversity is matched by a diversity in eruption styles and range of

79   volcanic deposits (Weaver et al., 1996; Kar et al., 1998; Hobson, 2001; Preece et al., 2016).

80   Evolved, more felsic, melts have the potential to generate significant hazards at ocean

81   island volcanoes, and thus understanding where and how they evolve in the crust is

82   imperative to forecasting future styles of eruption. The various means by which felsic

83   magmas evolve have the potential to produce a range of compositions, which affects

84   magmatic viscosity (Papale et al., 1998), and the amount of dissolved volatiles, all of which

85   contribute to the mode of evacuation of magma from crustal storage regions (e.g.

86   Eichelberger, 1995; Giordano et al., 2004). At ocean islands these silicic melts are

87   considered to be generated via: anatexis of crustal material by hotter mafic melts (e.g.

88   Sverrisdottir, 2007; Carley et al., 2011; Kuritani et al., 2011); extensive crystal fractionation

89   from a more primitive mafic magma (e.g.Geist et al., 1995; Mungall & Martin, 1995; Larrea

90   et al., 2014; Jeffrey et al., 2016); from direct derivation from mantle partial melting (Ashwal

91   et al., 2016) or through a combination of these processes (e.g. Bohrson & Reid, 1997;

92   Wiesmaier et al., 2013; Sliwinski et al., 2015). Understanding the relative importance of these

93   processes in any one setting has significant implications for understanding the relationships

94   between the timescales of magma genesis, magmatic heat flux and potential triggering

95   mechanisms of eruptions.

96   Ascension Island has produced more than 70 explosive eruptions of felsic magma in

97   its ~ 1 Myr subaerial history (Preece et al., 2016), in addition to numerous eruptions that

98   produced scoria cones, mafic lava flows, and felsic lava flows and domes. The erupted rocks

99   have largely been used to investigate the origins of Ascension Island magmatism (e.g. Harris

100   et al., 1982; Weaver et al., 1987, 1996; Weis et al., 1987; Kar, 1997; Kar et al., 1998; Paulick

101   et al., 2010). As yet, little is understood about the magmatic plumbing system on Ascension

102   Island and the control it exerts on magmatic composition and styles of eruptive activity. Thus,

103   we focus here on the relationship between the mafic and felsic magmatism on Ascension,

104   utilising whole rock major and trace element data, and a comprehensive suite of *in situ* crystal

105   major and trace element data by EPMA (electron probe microanalyses) and LA-ICPMS (laser

106   ablation inductively coupled plasma mass spectrometry). Samples studied here represent the

107   products of 22 eruptions representing the full range in composition and eruptive styles

108   presented by subaerial volcanism on Ascension Island. By combining these data with

109   previous isotopic work and work on a compositionally-zoned fall deposit (Chamberlain et al.,

110   2016), we present a model for the magmatic plumbing system of Ascension Island where

111   felsic magmas evolve and stall in the lower crust, and highlight the role of crustal structure in

112   the evolution of felsic melts on ocean islands with a low magmatic flux. Other potentially low

113   magmatic flux ocean islands include the archipelagos of the Azores and Cape Verde islands,

114   and thus the results of this study could be tested at other ocean islands around the world.

115

ASCENSION ISLAND

Ascension Island (7° 56' S; 14° 22' W) is located in the southern Atlantic Ocean, 90 km west of the Mid-Atlantic Ridge (MAR) and 50 km south of the Ascension Fracture Zone (AFZ; Fig. 1). Volcanism began on the sea bed 5 – 6 Myr ago, and subaerial volcanism has occurred from ~1 Ma to present (Kar et al., 1998; Minshull et al., 2010; Paulick et al., 2010; Jicha et al., 2013; Preece et al., 2016). The most recent eruption at Ascension Island has been dated using ^{40}Ar-^{39}Ar dating to 0.51 ± 0.18 ka (Preece et al., 2018) - with no evidence for pauses in eruptive activity of greater than 130 kyr throughout the 1 million years of subaerial volcanism (Jicha et al., 2013).

Crustal structure of Ascension Island

Ascension Island is built on 5 – 7 Myr old oceanic crust (Klingelhöfer et al., 2001; Paulick et al., 2010) on, or close to, the MAR. Due to the OIB-like trace element affinities of Ascension mafic lavas (Harris, 1983; Weaver et al., 1996), it has been suggested that magmatism at Ascension Island is the product of a shallow mantle plume, rising at the MAR then diverted along the Ascension Fracture Zone (AFZ, Fig. 1; Burke & Wilson, 1976; Montelli et al., 2006). However, seismic surveys have revealed a crustal structure that cannot be reconciled with a classic intraplate ocean island (i.e. a lack of lithospheric flexure, cf. Klingelhöfer et al., 2001), and instead suggest that significant growth of the Ascension Island edifice occurred on the MAR-axis. The seismic surveys show that the crust is 12 – 13 km thick under Ascension, with over-thickening of layer 3, to 7 km thick (Klingelhöfer et al., 2001). Active-source seismic tomographic studies failed to find evidence for magmatic underplating beneath the island, suggesting that the island's origins are not related to a hot spot (Evangelidis et al., 2004). Additionally, Evangelidis et al. (2004) located areas of anomalously high velocity

140 within the middle crust, which were inferred to be the crystallised remains of a relict magma

141 chamber.

142

143 **Geochemical insights into the source of Ascension Island**

144 OIB-like trace element patterns have been measured from magmas erupted on Ascension

145 Island, and spurred extensive research into the origins of magmatism, in particular its

146 relationship to an undefined mantle anomaly and the proximal MAR. Sr and Nd isotopic data

147 show little difference between the subaerial and the (volumetrically dominant) submarine

148 products of Ascension: ^{143}Nd/^{144}Nd varies between 0.51292 and 0.51310, and significant

149 variation in ^{87}Sr/^{86}Sr has been measured- between 0.70276 and 0.70656 (Fig. 2a; Weaver et

150 al., 1996; Kar et al., 1998; Paulick et al., 2010). Submarine products have distinctly different

151 Hf isotopic characteristics to the subaerial products studied here, and this has lead previous

152 workers to suggest that the mantle source tapped by the submarine stage is no longer present

153 (Fig. 2c; Paulick et al., 2010). There is little variation in Sr, Nd or Pb isotopic characteristics

154 with time in the subaerial edifice (Kar, 1997; Paulick et al., 2010; Jicha et al., 2013), nor is

155 the significant variation in ^{87}Sr/^{86}Sr coupled to variations in ^{143}Nd/^{144}Nd (Fig. 2a). The large

156 variation in ^{87}Sr/^{86}Sr has been suggested to reflect post-emplacement alteration of samples

157 (especially evolved rocks) by seawater-derived groundwater fluids as the samples were not

158 acid-leached prior to analysis (Kar et al., 1998; cf. Davidson et al., 1997). Due to the low Sr-

159 contents of the Ascension magmas, they are particularly susceptible to alteration either

160 through post-emplacement alteration, or by small degrees of assimilation of seawater-altered

161 lithologies (Kar et al., 1998).

162 Previous studies utilised the trace element variation in basaltic magmas erupted on

163 Ascension Island to infer source composition and to define three main magmatic groups,

164 principally based on Zr/Nb ratios (Weaver et al., 1996; Kar, 1997). The oldest and most

165   voluminous magma type in submarine and subaerial Ascension is represented by the high

166   Zr/Nb ($Zr/Nb > 5.7$) mafic lavas (principally exposed on the south coast, Fig. 1; Weaver et

167   al., 1996; Kar, 1997). Low Zr/Nb ($Zr/Nb < 4.3$) lavas are relatively spatially restricted,

168   outcropping only in the southwest (Fig. 1). Intermediate Zr/Nb lavas (Zr/Nb 4.3 – 5.7) are the

169   most common lavas in the subaerial history (but have erupted coevally with high and low

170   Zr/Nb lavas), and dominate the northern and western regions (Fig. 1; Weaver et al., 1996;

171   Kar, 1997; Jicha et al., 2013). The origins of these mafic lavas, and the process responsible

172   for their variation has been related to varying degrees of partial melting of a consistent

173   source, or melting of different mantle regions with differing mineralogy (Weaver et al., 1996;

174   Kar, 1997; Jicha et al., 2013). Isotopic and trace element data on the mafic lavas types

175   (Weaver et al., 1996; Kar et al., 1998; Paulick et al., 2010; Jicha et al., 2013), show that

176   fractional crystallisation alone cannot reproduce the variability in Ti, Ta and Nb (Fig. 2c),

177   and that variations in degree of partial melting, or source composition are more likely causes

178   of this variability (Jicha et al., 2013). As the Zr/Nb ratios are more characteristic of

179   variations during the initial production of magma (source lithology or degree of partial

180   melting), and will not be used here to investigate the nature of the magmatic plumbing

181   system.

182

183   **Evolution and distribution of volcanism at Ascension Island**

184   The magmatism on Ascension Island defines a transitional to mildly-alkaline, silica under-

185   saturated array from olivine basalt - hawaiite - mugearite - benmoreite - trachyte - rhyolite

186   (Daly, 1925; Weaver et al., 1996; Fig. 3). Mafic volcanic products are erupted all across the

187   island (Fig. 1), while felsic products are limited to central and eastern areas (Fig. 1). Previous

188   authors have divided the silicic eruptive products into two main centres: the older (Kar et al.,

189   1998; Hobson, 2001; Jicha et al., 2013) central felsic region, which contains the oldest dated

190   exposed lava on the island (at 1094 ka, Jicha et al., 2013), and the younger eastern complex

191   (youngest published Ar-Ar date of 52 ± 3 ka; Jicha et al., 2013; Fig. 1). Felsic magmas are

192   inferred to be the product of high degrees of fractional crystallisation (Fig. 2c; Weis et al.,

193   1987; Kar et al., 1998; Webster & Rebbert, 2001; Jicha et al., 2013) originating chiefly from

194   similar mafic melts to those erupted around the peripheries of the felsic complexes (both high

195   and intermediate Zr/Nb basalts have been suggested as parental melts; Figs. 1, 2c; Weaver et

196   al., 1996; Kar et al., 1998; Jicha et al., 2013).

197   The nature of the magmatic plumbing system on Ascension Island has not been

198   established, yet fractional crystallisation is suggested as the dominant process for the

199   formation of felsic melts (Kar et al., 1998; Jicha et al., 2013). There is only limited

200   geochemical evidence for interaction between evolved magma batches to date (Kar et al.,

201   1998; Chamberlain et al., 2016). Melt inclusion compositions and whole rock isotopic ratios

202   of plutonic lithic clasts have been used to infer a genetic association between the plutonic

203   lithics and the spectrum of volcanic rocks (Roedder & Coombs, 1967, Harris et al., 1982,

204   Weis et al., 1987, Webster & Rebbert, 2001). These studies have suggested that the formation

205   of the granitic plutonic bodies occurred at temperatures of 710 – 865 °C, and pressures of 200

206   – 300 MPa (Webster & Rebbert, 2001, and references therein). Recent work on the crystal

207   cargo and melt inclusions from a compositionally-zoned fall deposit on the island

208   (Chamberlain et al., 2016) supports the hypothesis that felsic magma evolved through closed-

209   system evolution on Ascension (as suggested by Harris, 1986, Weaver et al., 1987), with no

210   petrological or textural evidence for magma mixing or multiple phases of stalling. We test the

211   relevance of this model for the generation of all felsic magmas on Ascension Island, and use

212   these data to improve our understanding of the temporal and spatial relationships between

213   felsic and mafic volcanism.

214

SAMPLING & METHODOLOGY

The volcanic rocks on Ascension Island are extremely diverse and present evidence for Hawaiian, Strombolian and as well as more explosive (Subplinian to Plinian) eruptions, as well as phreatomagmatic activity. These products include lava flows and domes, pumice, scoria and ash fall deposits and pyroclastic density current deposits (Preece et al., 2016). The products of 22 representative eruptions that cover the full range in magmatic composition, eruptive style (Fig. 3) and the temporal and spatial extent of subaerial volcanism were analysed in detail to capture this range (Fig. 1; Table 1). Mafic lavas outcrop widely across the island and dominate its submarine history (see Nielson & Sibbett, 1996; Minshull et al., 2010). Mafic lava samples were selected to represent the main fields of mafic lava flows found on Ascension Island: the north coast (Sisters; samples AI14-411, AI14-471); the south-west region (Wideawakes; samples AI14-445, AI14-449); the south-east (Letterbox, AI14-423, AI14-429); the south coast (South Coast, AI14-514, AI14-522). In this way, the spatial and temporal variability (old vs. young lavas from the same eruptive centres) of mafic lavas on Ascension Island can be examined (Fig. 1; Table 1). Felsic samples come from effusive and explosive products, including samples from the older central felsic complex (AI-94, AI-103, AI15-621, AI14-459, AI14-488, AI14-493) and the younger eastern felsic complex (AI14-511, AI14-419, AI14-618, AI14-428, AI14-435, AI14-438). These samples were chosen to ensure a wide spatial and temporal sampling of the felsic volcanism (for individual sample names see Table 1).

Scoria and pumice samples were sieved to > 16 mm (or 8 mm if juvenile clasts were less than 16 mm) and all lithic clasts were removed by hand. These samples were then thoroughly cleaned by removing any adhering matrix or oxidised rind followed by soaking in (frequently changed) milli-RO water for a minimum of one week. Lava was treated by removing external, altered material then washed to remove any cutting fluid. All samples

9

240 were then dried thoroughly at 60 °C prior to crushing. An aliquot of each sample was selected

241 to mill for X-ray fluorescence (XRF) analysis at the University of East Anglia (UEA) using a

242 Brucker-AXS S4 Pioneer. For major elements (>0.5 wt.%) analyses of multiple international

243 standards yielded uncertainties $\leq \pm 0.5$ wt.% (2σ), except for SiO_2 which yielded

244 uncertainties of ± 1.06 wt.% (2σ). Values of the standards compared with published values

245 yielded accuracies within 2% for all major elements, except for MnO, CaO and P_2O_5 where

246 values were within 9% of published values; for full details of standards used, and their

247 precision see Electronic Appendix 1. Trace element analyses of selected standards gave

248 uncertainties < 5% (2σ) for V, Cr, Ni, Cu, Zn, Rb, Sr, Y, Zr, Nb, Mo and Ba, with

249 uncertainties <10% for As, Ce and U. For full details see Electronic Appendix 1.

250   The remaining material was prepared for *in-situ* analyses of major and trace elements

251 in crystals and glass. Thin sections were made of lava samples, whilst pyroclastic samples

252 were crushed, sieved into various size fractions (< 2 mm), before crystal and glass separates

253 (from the 0.5 – 1 mm size fraction), were hand-picked and mounted into low-activity epoxy

254 discs, and polished.

255   Prior to *in-situ* analyses, back-scattered electron (BSE) images were taken of all thin

256 sections and epoxy blocks to identify crystal phases present, any zonation preserved in

257 crystals and to locate suitable analytical spots. These images were obtained on a JEOL JSM

258 5900LV scanning electron microscope (SEM) at UEA. Percentages of phases were calculated

259 using ImageJ® software of transmitted light photomicrographs and BSE imagery, by filtering

260 images based on colour or greyscale characteristics.

261   *In-situ* major element analyses were obtained by EPMA using a JEOL JXA 8230

262 system at Victoria University of Wellington (VUW), or using a CAMECA SX100 at

263 Edinburgh University, both using wavelength-dispersive spectrometry. Operating conditions

264 varied depending on the phases and elements analysed, but precision of standard analyses of

265   major elements (>1 wt.% concentration) were always within 2 relative % (2 s.d.); with

266   slightly higher uncertainties for minor elements (see Electronic Appendix 1 for further details

267   on accuracy and precision of secondary standards). Due to their hydrous nature, only glass

268   analyses with totals of <93 wt.% were set aside; values for the remaining analyses were then

269   normalised to 100 %.

270   Trace element analyses of crystal phases and matrix glass were carried out at the

271   University of Durham using a New Wave deep UV laser (193 nm solid state) coupled to an

272   X-series 2 ICPMS (inductively-coupled plasma mass spectrometer). Analyses were run using

273   a 35 μm spot (for glass) or 50 μm spot (for crystals). The LA-ICPMS data were internally

274   normalized to ^{29}Si or ^{43}Ca from EPMA analyses. Abundances of single trace elements were

275   calculated relative to a bracketing standard (NIST 612) which was analysed throughout the

276   run under identical conditions. Precision and accuracies varied depending on the analytical

277   conditions but generally have <10% (2 s.d.) uncertainties (see Electronic Appendix 1 for full

278   details of precision and accuracy).

279

280   **RESULTS**

281   **Whole rock data**

282   The whole rock data confirm that the samples typify the full range in magmatic compositions

283   exposed on Ascension Island, from the least-evolved Green Mountain scoria sample (AI14-

284   552; 47.7 wt.% SiO_2, 3.01 wt.% Total Alkalis [TA]) through to the most-evolved sample of

285   1094 kyr-old (AI-94; Jicha et al., 2013) felsic lava (72.3 wt.% SiO_2, 10.3 wt.% TA; Fig. 3a,

286   Table 2). When selected whole rock trace element data are normalised to primitive mantle

287   (Palme & O'Neill, 2003) felsic lava and pumice samples are clearly depleted in Sr, Ti and Ba

288   relative to mafic lava and scoria samples (Fig. 3b). Felsic pumice and lavas are generally

289   more enriched in incompatible trace elements than the mafic lavas and scorias (Fig. 3b).

290   The whole rock data show increasing total alkalis, and decreasing CaO and MgO,

291   with increasing SiO_2 (Fig. 4). Mafic lavas are typically more-enriched in MgO, CaO and

292   TiO_2 (Fig. 4a, c), and depleted in FeO, Na_2O, K_2O, Zr and Ba (Fig. 4b, d, f, Table 3), relative

293   to felsic lavas. While having the textural characteristics of basaltic volcanism, samples of

294   Letterbox 'mafic' lavas are in fact intermediate, with 55.8 – 57.6 wt.% SiO_2, and 2.10 – 2.29

295   wt. % MgO. Pumice and felsic lava samples have similar major and trace element

296   concentrations (Fig. 3, 4), as do mafic lavas and scorias (Fig. 3, 4); thus there is no

297   appreciable difference in whole rock compositions between magmas erupted effusively or

298   explosively (Fig. 3, 4). Whilst there appear to be gaps within the MgO content (Fig. 4), these

299   solely reflect the samples selected for study, when compared with a large published data set

300   no gaps in composition are observed for Ascension Island volcanics (Fig.2c; Fig. 4 grey

301   fields).

302

303   **Petrology of Ascension lavas**

304   Mafic and intermediate lavas studied are generally crystal poor, with less than 5%

305   phenocrysts, apart from the samples from the South Coast (high Zr/Nb) lava with 18% and

306   40% phenocrysts in the two samples studied here (see Table 3, Fig. 5a, b). In the mafic and

307   intermediate lava flows, phenocrysts (> 500 μm) are predominantly plagioclase feldspar (Fig.

308   5c, d), with minor olivine in some samples (Table 3, Fig. 5). Phenocryst phases in the crystal

309   rich lavas (from the South Coast) are larger, up to 5mm, modal size 3mm, when compared

310   with all other mafic and intermediate phases, where phenocrysts are generally < 1mm in

311   diameter. The groundmass of all mafic and intermediate lavas studied here is

312   microcrystalline, with no glass present. The groundmass consists of plagioclase feldspar,

313   clinopyroxene, olivine and Fe-Ti oxides (Fig. 5a-d, Fig. 6) in decreasing order of abundance.

314   Felsic lava samples come from the (older) central felsic complex (AI14-103, AI15-

315   621, AI-94; Fig. 1) and the (younger) eastern felsic complex (AI14-511, AI14-485, AI14-

316   419, AI14-428). All felsic lavas are crystal poor, with <6% phenocrysts visible in hand

317   sample (Table 3). Phenocrysts phases are dominantly ternary feldspars (plagioclase to alkali-

318   feldspars, Fig. 7), with minor Fe-Ti oxides and aegirine-augite present as phenocrysts phases

319   in two samples (Table 3). Phenocrysts are always <3 mm diameter. In thin section, crystals

320   are largely euhedral, and feldspar crystals often present as clots of 2-5 crystals (Fig. 5e-h; Fig.

321   6d, e). The groundmass is usually microcrystalline, consisting of ternary feldspar, cristobalite,

322   interstitial aegirine-augite and Fe-Ti oxides in decreasing order of abundance (Table 3; Fig.

323   6d, e, f). A single felsic lava sample has a glassy matrix (AI14-419, the Letterbox felsic lava

324   sample), which has SiO_2 concentrations between 71.2 and 74.0 wt.% (Table 3; Fig. 11).

325

Mineral compositions of the mafic and intermediate lavas

327   Plagioclase feldspar is a dominant mineral phase in all mafic and intermediate lavas with

328   compositions varying between $An_{37}Ab_{61}Or_2$ and $An_{82}Ab_{17}Or_1$ (Fig. 7). BSE images of

329   feldspar crystals typically show faint oscillatory zoning (Fig. 6c) with the South Coast (high

330   Zr/Nb) lavas having better developed zonation and resorbed cores (Fig. 6a, b). The lack of

331   well-developed BSE image zonation patterns in the Sisters, Wideawakes and Letterbox

332   feldspars (mafic lava fields, see Fig. 1 for name origins) is reflected in their major and trace

333   element compositions which show limited variations (Fig. 7, 8). The South Coast lavas

334   exhibit some compositional variation between core and rims in their feldspar population (Fig.

335   8c, 9a), with cores typically being less-evolved than feldspar rims. Olivine compositions in

336   the groundmass (or as phenocrysts in South Coast and Wideawakes samples) vary between

337   Fo49 – Fo89. Where groundmass olivine can be identified separately to phenocrysts,

338   groundmass olivines have higher CaO and lower MnO concentrations at any given value of

339 Fo number. Olivine crystals are faintly normally-zoned, if they are zoned at all, with no

340 evidence for resorbed cores in any samples studied (Fig. 6a, b, 9b, 10).

341   No variation is seen in phenocryst compositions between the stratigraphically older

342 and younger samples from the same geographic regions. However, some variation in mineral

343 compositions exists between different geographic regions, with differences in major and trace

344 elements between geographic regions (Fig. 8a, c). Letterbox samples have more restricted

345 feldspar and olivine compositions, representing the more-evolved end of the range in mineral

346 compositions displayed by all mafic lavas (Fo 56 – 69; An 36 – 47; Fig. 8a; Figs. 9, 10a,

347 10c), consistent with their whole rock compositions (see Table 2). South Coast, Sisters and

348 Wideawakes lavas generally contain more variable An-plagioclase (An 32 – 82; see Table 5,

349 Fig. 1, 8, 9), which has lower Sr concentrations (and extends to higher anorthite contents; Fig.

350 8a, c), and more variable olivine (that extends to less-evolved compositions) than Letterbox

351 (Fo49 – Fo89; Table 5, Fig. 1, 9, 10), consistent with their less evolved whole rock

352 compositions.

353

354 **Mineral compositions of the felsic lavas**

355 Ternary feldspar is the dominant mineral phase in all felsic lavas with compositions varying

356 between $An_{20}Ab_{75}Or_5$ and $Ab_{70}Or_{30}$ (Fig. 7). BSE images of feldspar crystals from felsic lava

357 samples are unzoned (Fig. 6d, e). However, some lava flows show core-rim-groundmass

358 variations in feldspar compositions (see Fig. 8c and Electronic Appendix 2), which is

359 unresolvable in BSE images alone. In particular, sample AI14-485 (from the eastern felsic

360 complex; Fig. 1) has systematically more-evolved rims than cores, and more-evolved

361 groundmass than rims. Feldspar compositions of felsic lavas range from andesine

362 ($An_{20}Ab_{75}Or_5$) through to anorthoclase ($Ab_{70}Or_{30}$; Fig. 7, Table 4), with the most-evolved

363 compositions ($Ab_{70}Or_{30}$) present in both the older and younger felsic samples (see Fig. 8b;

14

364 Electronic Appendix 2). Most felsic feldspars (that are ternary) define a separate trend to the

365 mafic and intermediate lava samples (with plagioclase feldspar only), having higher

366 concentrations of Eu and Ba at any given Sr concentration. (Fig. 8d). Aegirine-augite is

367 present as a groundmass phase in all felsic lava samples studied here, with compositions

368 between $0.5 - 12.1$ wt.% Na_2O and $0.1 - 6.2$ wt.% MgO. Aegirine-augite, typically < 500 μm

369 (Fig. 11), commonly contains Fe-Ti oxide inclusions, and has higher Mn and lower Sr

370 concentrations than the intermediate lavas (Fig. 11c), whilst the minor olivine ($< 1\%$), present

371 only in the Letterbox felsic lava, is $Fo12.5$ (see Electronic Appendix 2).

372   The crystal compositions between samples of felsic lavas and samples of mafic to

373 intermediate lavas do not overlap in their major elements. The samples from the younger

374 eastern felsic complex (Fig. 1) have the greatest range in both feldspar ($An_{20}Ab_{75}Or_5 -$

375 $Ab_{70}Or_{30}$) and clinopyroxene compositions ($0.5 - 12.2$ wt.% Na_2O; Fig. 8b, 11a, b, Table 5,

376 7), while crystals within samples from the central felsic complex are typically more-evolved;

377 containing anorthoclase feldspar ($An_7Ab_{73}Or_{20} - Ab_{70}Or_{30}$) and more aegirine-rich

378 clinopyroxene ($2.9 - 9.0$ wt.% Na_2O; Fig. 11a, b; Table 7).

379

380 Petrological variation in mafic pyroclastic deposits

381 Pyroclastic deposits are exposed all across the island and have compositions ranging from

382 basalt to rhyolite, with no obvious Daly Gap when all published samples are considered

383 (Daly, 1925, Fig. 3, 4). The scoriaceous deposits studied here are crystal poor, with

384 phenocrysts of plagioclase feldspar and minor olivine, clinopyroxene and Fe-Ti oxides. The

385 Green Mountain scoria (AI14-552) is a relatively voluminous eruption, with widespread

386 deposits originating from within the central felsic complex. Its key identifying feature is the

387 presence of abundant white-cream plutonic lithic clasts. In thin section, juvenile scoria

388 typically contains plagioclase feldspar + olivine $\pm$ clinopyroxene $\pm$ Fe-Ti oxides. The

389 groundmasses of the scoria clasts from these deposits have varying proportions of microlites

390 (feldspar + olivine).

391   In BSE imagery, crystal phases are not zoned, and preserve euhedral crystal habits.

392 Feldspar compositions overlap those of both the mafic and felsic lavas, ranging between

393 $An_{14}Ab_{72}Or_{14}$ and $An_{84}Ab_{15}Or_1$. The Green Mountain scoria has the largest variation in

394 feldspar compositions (AI14-552; Table 5), but there are no systematic differences in core

395 and rim compositions of individual crystals (Fig. 8c, Table 5). Olivine, the other major

396 phenocrystic phase, overlaps compositionally with olivine in the mafic lavas, with Fo74 to

397 Fo87 (Fig. 9b, 10b; Table 6) and also has no systematic difference in core and rim

398 compositions from individual olivines (Fig. 10c). Matrix glass compositions are typical of

399 mafic melts, with low SiO_2 (< 50 wt.%) and high CaO (> 6 wt.%), (Fig. 12, Table 8); the bulk

400 scoria composition is slightly less-evolved (45.8 – 49.3 wt.% SiO_2) than the NE Bay scoria

401 (AI14-438, 49.0 – 52.4 wt.% SiO_2).

402

403 **Petrological variation in felsic pyroclastic deposits**

404 Pumice clasts are typically crystal poor, with < 5% crystals. Ternary feldspar is the dominant

405 crystal phase (oligoclase to anorthoclase composition ± sanidine) with one ferromagnesian

406 phase of either amphibole or fayalitic olivine, with minor magnetite ± ilmenite ± apatite, and

407 rarely augitic clinopyroxene is present. One exception to this is the intermediate sample

408 AI14-459 which has ~15% crystals, with large amphibole (up to 3 mm) phenocrysts. Crystal

409 phases are not zoned in BSE, and preserve euhedral crystal habits. Groundmass is typically

410 glassy, with varying amount of feldspar microlites.

411   Feldspar compositions from these pumice fall deposits intersect and straddle those

412 from the evolved effusive eruptions (Fig. 7, Table 4): with compositions ranging between

413 $An_{51}Ab_{47}Or_2$ and $An_{0.5}Ab_{58.5}Or_{41}$. Some eruptions have relatively restricted feldspar

16

414   compositions (e.g. AI14-488: $An_{0.5}Ab_{65.5}Or_{34} – An_1Ab_{69}Or_{30}$) whereas other extend over wide

415   ranges (e.g. AI14-435: $An_2Ab_{73}Or_{25} – An_{18}Ab_{76}Or_6$). In trace elements, the felsic pyroclastic

416   feldspars plot within the higher- and lower-Eu trend (Fig. 8d). No clear core-rim relationships

417   were found in feldspar compositions: only one pumice fall deposit in Middleton's Valley

418   (AI14-459) has slightly less-evolved cores relative to rim compositions (cores: $An_{51}Ab_{47}Or_2 –$

419    $An_{20}Ab_{74}Or_6$; rims $An_{43}Ab_{54}Or_2 – An_{20}Ab_{74}Or_6$). This comparatively crystal-rich sample (see

420   Table 3) also bridges the divide between our felsic and mafic lava feldspar populations.

421   Fosterite content in olivines ($Fo1 – 57$) from felsic pyroclastic samples mirrors the

422   relationships between pyroclastic and effusive lava feldspars- intersecting with and extending

423   the range in compositions of mafic lava sourced olivines (Fig. 10b, Table 6). Again, no

424   differences between core and rim compositions are observed in olivine from all pyroclastic

425   samples (Fig. 10c).

426   Glass compositions of felsic pyroclastic deposits range from ~ 66 wt.% to 75 wt.%

427   SiO_2 (Fig. 12; Table 8). All sampled pyroclastic deposits have relatively homogenous glass

428   compositions, with the one exception being the glass from the compositionally-zoned fall

429   deposit, previously described in Chamberlain et al. (2016; Fig. 12a). In detail, individual

430   sample variation in trace elements shows up to a four-fold variation in elements compatible in

431   feldspar (Ba, Sr; Fig. 12b). However, limited variations in source-related trace elements (such

432   as Th/U ratio; Fig. 12c) are evident between samples, where variation within a single sample

433   is of the same magnitude or greater than variations between samples.

434

435   **Intensive variables**

436   Where available, two co-existing oxides (magnetite and ilmenite) were analysed and Fe-Ti

437   oxide thermometry of Ghiorso & Evans (2008) was applied (if the pairs passed the

438   equilibrium test of Bacon & Hirschman, 1988). Iron-titanium oxide derived temperatures

439   range from 932 °C to 1037 °C for the mafic lavas (Table 8). Oxygen fugacity varies between

440   –0.45 log units relative to the Nickel-Nickel Oxide (Δ NNO) buffer to +0.05 log units Δ

441   NNO. Felsic lavas and pyroclastic samples yield Fe-Ti oxide temperatures ranging from 850

442   °C to 960 °C, and fO_2 ranging from –0.5 log units Δ NNO to –2.3 log units Δ NNO (Table 8).

443   Plagioclase-melt thermometry (Putirka, 2008) and alkali feldspar-melt thermometry

444   (Putirka, 2008) was applied to all samples where equilibrium between feldspars and melt

445   could be established (Putirka, 2008). Pressures of 330 MPa were assumed for mafic samples,

446   as this is consistent with equilibration at the base of the crust, (Klingelhöfer et al., 2001) and

447   pressures of 250 MPa were used for felsic samples, based on melt inclusion entrapment

448   pressures modelled from samples of a zoned fall deposit on Ascension Island (Chamberlain et

449   al., 2016). This modelling yielded temperatures within a similar range (but often higher) to

450   that of the Fe-Ti oxide thermometry (Table 8) with modelled temperatures ranging between

451   772 °C and 1034 °C for felsic samples, and between 1093°C and 1174 °C for mafic samples

452   (Table 8). Although a specific pressure was assumed, testing demonstrated that the pressure

453   effect is minimal, with less than 10 °C variation in estimated temperatures with > 200 MPa

454   variation in assumed pressures.

455   Using measured alkali feldspar-melt compositions and temperatures modelled from

456   plagioclase-melt thermometry, the alkali feldspar-melt hygrometer of Mollo et al. (2015) was

457   also applied (see Table 8 for summarised results, full results in Electronic Appendix 2).

458   Calculated water concentrations are high (average concentrations for the felsic units between

459   4.66 wt.% and 8.12 wt.%, Table 8). Modelled water contents associated with the felsic lava

460   and dome samples have consistently lower water concentrations than the explosively erupted

461   samples. These high concentrations of water in explosive felsic samples are similar to those

462   measured in Ascension Island melt inclusions (Chamberlain et al., 2016) and with the high

463   loss on ignition from felsic pyroclastic samples measured during XRF analyses (see

464   Electronic Appendix 2 for full XRF results).

465

466   **DISCUSSION**

467   **Origin of compositional variations in Ascension Island magmas**

468   A range in whole rock and crystal compositions are evident in Ascension Island samples,

469   with no clear differences observed between effusively erupted lava samples and explosively

470   erupted pumice and scoria samples (Fig. 4, 7a). When considered alone, the variations in

471   whole rock chemistry presented here (Fig. 4) do not give reason to disagree with previous

472   whole rock studies of Ascension Island, which have suggested that fractional crystallisation is

473   the dominant mechanism for producing evolved melts (e.g. Harris, 1983; Kar et al., 1998;

474   Jicha et al., 2013; Chamberlain et al., 2016), evidenced by the continuous trend in major and

475   trace element concentrations (Figs. 3, 4; Weaver et al., 1996; Kar et al., 1998; Jicha et al.,

476   2013), and the lack of whole rock radiogenic isotopic ratio variation with major element

477   concentrations (Fig. 2d; Weaver et al., 1996; Kar et al., 1998; Paulick et al., 2010).

478   Partial melting of mafic material is another process through which felsic melts have

479   been proposed to be generated at ocean island volcanoes (e.g. Borhson & Reid, 1997;

480   Sverrisdottir, 2007; Carley et al., 2011; Kuritani et al., 2011). Unlike other ocean islands,

481   there is no evidence for divergence in Nd isotopic ratios between mafic and felsic melts (Kar

482   et al., 1998), and major and trace elements vary co-linearly (Fig. 2b; Kar et al., 1998; Jicha et

483   al., 2013) which previous studies suggest is not supportive of a partial melting origin for

484   evolved melts at Ascension. Some minor assimilation and contamination has been inferred to

485   be partly responsible for the radiogenic Sr isotopic compositions of more felsic melts (Kar et

486   al., 1998), but this cannot be quantified based on the new data presented here, and it is noted

487   that none of the earlier isotopic data was acid leached prior to analysis (cf. Davidson et al.,

488   1997). At other volcanic systems where partial melting has been shown to be a significant

489   driver for the production of evolved magmas, magmatic compositions can be bimodal, with

490   few erupted magmas of intermediate composition (e.g. Charlier et al., 2013, Meade et al.,

491   2014), which is not observed at Ascension (Fig. 3, 4). However, small degree direct partial

492   melting of a seawater-altered basaltic/gabbroic parent cannot be ruled out with our new data

493   set for Ascension (cf. Kar et al., 1998), and may be responsible for some of the variation in

494    $^{87}Sr/^{86}Sr$ isotopic ratios (Fig. 2a).

495   Magma mixing between mafic and felsic magmas to produce the intermediate rocks

496   could be responsible for the continuum in whole rock compositions at Ascension (Fig. 3), yet

497   non-linear variations in major and trace elements in both whole rock compositions (especially

498   in TiO_2, K_2O and Zr, Fig. 4) and crystal phases (Fig. 8d, 10d) suggest that this is unlikely.

499   Similarly, crystal compositions form coherent trends within individual samples, with no

500   evidence for the distinct populations (cf. Geist et al., 1995; Troll & Schminke, 2002; Fig. 8 –

501   11) that could represent growth in different magmas. Petrographic data shows no evidence of

502   magma mixing, therefore fractional crystallisation is hypothesised to be the main mechanism

503   for generation of felsic melts at Ascension Island, in agreement with previous authors (cf. Kar

504   et al., 1998; Jicha et al., 2013).

505   To test the fractional crystallisation hypothesis further, MELTS modelling of isobaric

506   liquid lines of descent (Gualda & Ghiorso, 2015) from the least evolved sample (AI14-438,

507   see Table 1) has been undertaken at a range of pressures, from 330 MPa (the base of the

508   crust, Klingelhöfer et al., 2001) to 90 MPa (~ 3.5 km depth), as well as an isothermal

509   decompression model from 90 MPa to 1MPa (Fig. 13, 14). An initial starting composition

510   from AI14-438 was used, with an assumed water concentration of 0.5 wt.% H_2O, and fO_2 at

511   the NNO-buffer based on Fe-Ti oxide thermometry (Table 8) and analyses of nearby MAR

512   glasses (Almeev et al., 2008) which tap a mixed enriched Ascension Island-type source and a

513   depleted high εHf mantle (Paulick et al., 2010). It has been shown that oxygen fugacity is not

514   solely fractionation dependent at Ascension Island (Chamberlain et al., 2016) and this one-

515   step MELTS modelling does not properly reflect the fractionating phases at the more-evolved

516   end. Thus, at T< 950 °C the composition of AI15-621 was used, the least-evolved of the

517   felsic lava samples, with an assumed water concentration of (5.1 wt.% H_2O) from feldspar-

518   melt hygrometry, and fO_2 -1.5 ΔNNO from Fe-Ti oxide thermometry (Table 8).

519   The modelled liquid lines of descent of this two-step MELTS modelling reproduce the

520   observed variations in whole rock composition (Fig. 13), with the models run at higher

521   pressure (250 MPa or greater) having a better fit for MgO and CaO concentrations (Fig. 13b,

522   c), suggesting fractionation at depths of more than 7 km. At the more evolved compositions

523   (>68 wt.% SiO_2), fractionation at 170 MPa better reproduces the more evolved compositions

524   of Ascension Island magmas (Fig. 13a). Whilst isobaric fractionation is unlikely to occur at

525   Ascension Island, the MELTS modelling shows that simple fractional crystallisation can

526   replicate the observed variations in whole rock composition, when oxygen fugacity can be

527   controlled to represent that measured in Ascension Island magmas. Similarly, modelled

528   increases in H_2O with increasing SiO_2 support the modelled high melt H_2O concentrations

529   from feldspar-melt hygrometry (Table 8), especially at higher pressures of evolution (Fig.

530   13d).

531

532   *Fractional crystallisation in mafic and intermediate magmas*

533   Fractional crystallisation, as modelled by MELTS, has demonstrated that the observed whole

534   rock compositional range within the Ascension Island magmatic suite can be reproduced in

535   this process. For the mafic and intermediate magmas, the crystal compositions measured

536   overlap well with the modelled crystallising phases from MELTS (Fig. 14), and up to 70%

537   total fractionation has occurred to produce the most evolved intermediate magmas (Fig. 13).

538   Whilst MELTS details proportions of phases fractionating, previous studies have

539   demonstrated some limitations on the model's ability to accurately predict crystallisation of

540   water-bearing phases (Gualda et al., 2012), clinopyroxene (Fowler & Spera, 2010) and apatite

541   (Rooney et al., 2012). Therefore, to yield further insights into proportions of phases

542   crystallising least-squares modelling of the major elements has been undertaken, constrained

543   by using only phases observed in samples of Ascension Island volcanics.

544   Major element least-squares modelling was carried out using Petrograph (Petrelli et

545   al., 2005, built on the least-squares modelling of Stormer & Nicholls, 1978), and to include

546   entrainment where appropriate (cf. Kar et al., 1998, Electronic Appendix 3). A comparison of

547   phases crystallising at each modelled stage between MELTS and Petrograph can be seen in

548   Electonic Appendix 3. Two stages of evolution are considered initially, to attempt to

549   reproduce the variations in mafic to intermediate whole rock compositions (Fig. 3): Stage 1)

550   from the NE Bay Scoria (the most primitive basalt; AI14-438) to the Wideawakes (an

551   intermediate Zr/Nb basalt marking the inflection in MgO vs TiO_2, Fig 4c; AI-445); Stage 2)

552   Wideawakes (AI14-445) to Letterbox (the intermediate lava; AI14-423). In both stages,

553   compositions of plagioclase feldspar, olivine, clinopyroxene, ilmenite and magnetite

554   measured in the parent sample were used. Apatite was also used as an accessory phase, given

555   its presence as inclusions in mineral phases and the variation in P_2O_5 evident in whole rock

556   data (Table 2; full details of modelling conditions see Electronic Appendix 3). Whilst this

557   modelling is limited by the assumption of uniform compositions of the fractionating phases,

558   and has no pressure or temperature dependence, it provides a first order constraint on modal

559   fractionating assemblage provided the sum of the squared residuals is < 2 (Stormer &

560   Nicholls, 1978). Stage 1 fractionation modelling (sum of squared residuals [SSR] 0.25)

561   suggests that ~ 8% fractionation of an assemblage dominated by plagioclase feldspar with

562   subordinate olivine and apatite, coupled with the minor entrainment (4%) of clinopyroxene

563 and two oxides could produce the compositions of AI-445. The second stage of modelling

564 (SSR 0.05), to produce the intermediate Letterbox magmas, suggests a further 56%

565 fractionation (0.4 melt fraction remaining) of an assemblage dominated by feldspar and

566 clinopyroxene, with minor olivine, magnetite, ilmenite and apatite (See Electronic Appendix

567 3 for graphic representation; and comparison with modelled MELTS fractionating phases).

568   These modelled fractionating assemblages have been further tested using published

569 distribution coefficients for Rb, Sr, Y, Zr, Nb and Ba in the fractionating phases (Fig. 15, full

570 details and references for the distribution coefficients used is given in Electronic Appendix

571 3). Generally fractional crystallisation (excluding any accumulation) can reproduce observed

572 variations in Rb, Nb, Ba and Zr, with a poorer agreement with Sr and Y data (Fig. 15 and

573 Electronic Appendix 3) for the variation observed in mafic magmas.

574

575 *Felsic magma evolution*

576 Felsic magma evolution through closed system fractional crystallisation, modelled by

577 MELTS, is shown to reproduce well the major elements of the whole rock data for Ascension

578 in most elements (Fig. 13), and pressure of fractionation has a significant effect on total

579 alkalis (Fig. 13a) reflecting the pressure-sensitivity of feldspar crystallisation (Fig. 14a).

580 Fractionating assemblages again reproduce well the measured compositions of feldspar,

581 olivine and clinopyroxene. In the more-evolved lavas, growth of low-pressure phases

582 (evidenced by feldspars with ~4 – 6 wt.% K_2O and Na-rich clinopyroxenes, Fig. 14a, c)

583 reflect growth at a range of pressures (cf. isothermal decompression crystal compositions

584 from MELTS modelling; Fig. 14) which are not observed in equivalent explosive deposits.

585   Again, to supplement the MELTS modelling, major element least-squares modelling

586 was carried out using Petrograph (Petrelli et al., 2005; from Stormer & Nicholls, 1978). Two

587 further stages of evolution are considered, to attempt to reproduce the trends observed in

588   whole rock concentrations (Fig. 3): Stage 3) Letterbox (AI14-423) to Devils Riding School

589   (representative of the trachytic lavas on Ascension, Fig 3; AI15-621) and Stage 4) Devils

590   Riding School (AI15-621) to Middleton's Ridge (most-evolved rhyolite, AI-94). In both

591   stages, compositions of feldspars (plagioclase and ternary feldspar), olivine, clinopyroxene,

592   ilmenite and magnetite measured in the parent sample were used. Apatite was also used as an

593   accessory phase, given its presence as inclusions in mineral phases and the variation in P_2O_5

594   evident in whole rock data (Table 2; full details of modelling conditions see Electronic

595   Appendix 3).

596   Stage 3 (SSR 1.23) requires a further 60% fractionation (0.16 melt fraction remaining

597   from initial mafic starting sample) of an assemblage again dominated by plagioclase feldspar,

598   with subordinate clinopyroxene, apatite, ilmenite, and minor entrainment of magnetite (1%).

599   Contrastingly, MELTS modelling suggests both biotite and orthopyroxene should begin to

600   fractionate (neither of which have been observed on Ascension Island, Electronic Appendix

601   3). Stage 4 (SSR 0.08) shows a clear change in fractionating assemblage with ternary feldspar

602   dominating the fractionating assemblage with clinopyroxene and magnetite, and requiring a

603   further 57% fractionation (0.07 melt fraction remaining, in agreement with MELTS

604   modelling of liquid lines of descent: 0.06 melt fraction remaining, Fig. 13). Minor

605   accumulation (4%) of fayalite, ilmenite and apatite contributes to the evolution of the felsic

606   magmas (see Electronic Appendix 3). These inferred fractionating phases are in good

607   agreement with the observed crystal phases present in Ascension samples with feldspar being

608   the dominant crystal phase present, with minor fayalitic olivine or clinopyroxene present,

609   unlike MELTS modelling which again fails to accurately reproduce the observed mineral

610   phases, with the suggested presence of leucite and orthopyroxene (Table 3, Electronic

611   Appendix 3).

612   Trace element modelling of the proposed fractionating assemblages was undertaken

613   for stages 3 and 4, again excluding any accumulation of phases. The results of this modelling

614   show that Ba is successfully modelled by this fractionating assemblage, with moderate but

615   less consistent results for modelled vs. measured Sr and Nb (Fig. 15, Electronic Appendix 3).

616   There is poor agreement between modelled and measured Zr, Rb and Y (Fig. 15, Electronic

617   Appendix 3). Zircon is observed in the most evolved samples, but fractionation of this phase

618   has not been modelled as the proportions are challenging to quantify using major element

619   modelling, although it could be the cause of the variations between observed and modelled

620   concentrations of Zr and Y in the felsic magmas of Ascension. We note that accumulation or

621   fractionation of minor phases, whilst not significant in terms of the major element evolution

622   of the felsic melts, can significantly affect the trace element compositions of melts. With a K_d

623   of ~ 40 in rhyolitic apatites (Pearce & Norry, 1979), Y concentrations will be significantly

624   affected by even minor amounts of fractionation of this phase.

625

626   *The role of ascent rate and oxygen fugacity*

627   Use of MELTS modelling to yield crystal compositions has highlighted the role of crystal

628   growth in the upper crust during ascent in the presence or absence of phases in the felsic

629   magmas. Moderate 4 – 6 wt.% K_2O feldspar and aegirine-augite are only found in felsic

630   lavas; in felsic pyroclastic samples no feldspar has 4 – 6 wt.% K_2O and fayalite is the

631   common 'mafic' phase (Fig. 10b)- rare clinopyroxene is augitic in composition, and reflects

632   fractionation at pressures ≥ 90 MPa (Fig. 14c). Pyroclastic samples have high modelled water

633   concentrations (Table 8) perhaps reflective of higher pressure storage (Fig. 13d, cf. Di Matteo

634   et al., 2004; Brenna et al., 2014). Combining the lack of chemical zonation (Figs 9c, 10c), the

635   euhedral nature of the phenocryst phases (Fig, 6), and no low-P phases forming (cf. Fig. 14c),

636   ascent rates for pyroclastic magmas, fractionating at high pressures ($\geq$ 250 MPa, c.f. Fig. 13)

637   is likely to be rapid and warrants further comparison with their effusive counterparts.

638   In other alkaline systems it has been shown that variations in fO$_2$ at constant

639   temperatures can result in variable phase assemblages (White et al., 2009; Markl et al., 2010).

640   Given the large variation in calculated fO$_2$ within Ascension Island magmas (Table 8), some

641   of the small variation around liquid lines of descent, and mismatch between the MELTS-

642   modelled vs. observed phases, may stem from variable phase crystallisation at differing fO$_2$

643   conditions, as well as variations in ascent rate and depth to storage regions within the lower

644   crust.

645

646   **Spatial and temporal variations in magmatism at Ascension Island**

647   *Temporal and spatial variation of mafic magmas*

648   Whole rock major and trace element data and crystal compositions show little variation

649   between samples of older and younger lavas (Table 2, Fig. 4) from the same eruptive centres,

650   suggesting that the mode of mafic magma generation and ascent has been relatively constant

651   for the subaerial (and exposed) history of Ascension Island. This is in agreement with

652   previous whole rock isotopic data, which shows no clear variation in the subaerial edifice of

653   Sr, Nd or Pb isotopic ratios over time, indicative of source characteristics (Weaver et al.,

654   1996; Kar, 1997; Paulick et al 2010; Jicha et al., 2013). While there is no temporal variation

655   in the composition of mafic subaerial magmas erupted on Ascension, there are significant

656   spatial differences in the phenocryst percentages, whole rock compositions, and crystal

657   compositions, depending on the location of the eruptive centre (detailed in Table 1; Table 3,

658   Figs. 4, 8, 10). South Coast lavas have the highest crystal contents (>17 %) and the least-

659   evolved crystal compositions (down to An82, and Fo87; Fig 8, 10), whereas the Letterbox

660   samples from the SE of the island are intermediate in composition, contain clinopyroxene as

661   a minor component (instead of olivine; Table 3), and more restricted feldspar compositions.

662

663   *Origin of the crystal cargo*

664   Given the marked differences in crystallinity between the South Coast lavas (AI14-522 and

665   AI14-514; Table 1) and the other mafic to intermediate lavas (Table 3), modelling of

666   plagioclase and olivine equilibrium compositions, based on the whole rock compositions at

667   an assumed temperature and pressure, following the method of Price et al. (2012), was

668   undertaken (Fig. 9). The range in olivine Mg# from different eruptive centres (Fig. 9) shows

669   that not all of the olivine crystal cargo is modelled to be in equilibrium with the melt in which

670   it is erupted (Fig. 9b). Rim analyses are just as likely to be in disequilibrium with the whole

671   rock compositions as core analyses. This range in olivine Mg# shows that some crystals are

672   not phenocrystic, despite the lack of significant overgrowths and the crystals mostly having a

673   euhedral to subhedral habit (Fig. 6).

674   Similarly, plagioclase feldspar compositions are not in equilibrium with their whole

675   rock compositions (Fig. 9a) and yet only feldspars from the South Coast lavas display

676   reaction rims and anhedral cores (Fig. 6b). Whilst the calculation of equilibrium plagioclase

677   compositions (following the method of Panjasawatwong et al., 1995) is only calibrated for

678   plagioclase feldspar compositions (and not in alkaline systems such as Ascension), and thus

679   could be a potential reason for why feldspars are in apparent disequilibrium, single samples

680   preserve a wide variation in An content in the feldspars, showing that irrespective of the

681   modelled equilibrium conditions, significant amounts of feldspar crystals will not be in

682   equilibrium with their host rock composition.

683   Mafic lavas, excluding those from the South Coast group, are clearly in chemical

684   disequilibrium with their feldspars, with less variation from the calculated equilibrium

685 composition for olivines (Fig. 9). Densities of the mafic magmas were calculated following

686 the method of Bottinga & Weill (1970), at pressure of 330 MPa (the base of the crust

687 (Klingelhöfer et al., 2001) using measured whole rock compositions and a water

688 concentration of 0.5 wt.%. Densities of mafic magmas are on the order of 2.7 g/cm^3,

689 remarkably similar to that of plagioclase feldspar (2.6 – 2.7 g/cm^3, Scoates, 2000; Ghiorso &

690 Gualda, 2015), yet less dense than olivine and clinopyroxene, (~3.6 g/cm^3 and ~3.2 g/cm^3

691 respectively, Scoates, 2000; Ghiorso & Gualda, 2015). Thus, fractionating feldspar in a zone

692 of magma storage will not sink, and instead may form lateral mushy cumulates as the magma

693 evolves, whereas olivine and clinopyroxene have bigger density differences with the mafic

694 magmas, and thus can sink more effectively. As the mafic magma reaches eruptible

695 conditions, either due to concentration of volatiles within the magma (e.g. Stock et al., 2016),

696 tectonic destabilisation of the system (e.g. Allan et al., 2012) or through gas injection (e.g.

697 Caricchi et al., 2018), the mafic magma rapidly incorporates these lateral mushy feldspar

698 antecrysts, producing the wide range in feldspar compositions found within single eruptions,

699 that are in disequilibrium with their whole rock composition, yet native to the magmatic

700 system (Fig. 9a, 14a). The timescale of incorporation of these antecrystic crystals prior to

701 eruption must be short, as no zonation is observed (see Figs. 8 – 10), and feldspars generally

702 retain their euhedral appearance (Figs. 5, 6). Similarly, the mushy storage regions in which

703 the feldspars and mafic phases are forming are transient; no evidence is preserved for long-

704 lived melt-dominant magma storage regions for mafic to intermediate magmas, with no

705 evidence for incorporated crystals seeing more than one 'triggering' event (cf. Kahl et al.,

706 2013).

707   *Role of crystal entrainment in mafic to intermediate magma genesis:* Excluding the

708 South Coast group lavas, all other mafic and intermediate lavas have crystallinities less than

709 5% (Table 3), with limited evidence for chemical zonation (Fig. 10c) and euhedral crystal

710 habits (Fig. 4, 6), thus incorporation of mushy antecrysts (which are subsequently resorbed)

711 appears unlikely to constitute more than 5% (total rock crystallinity) of the rock volume. The

712 similarities in antecrystic and phenocrystic crystal cargo in Ascension Island lavas make

713 assessing the proportions of assimilated material challenging, as incorporation of these

714 antecrysts may merely shift the whole rock compositions along the modelled liquid line of

715 descent. This has implications for modelling the total amount of fractional crystallisation

716 responsible for individual mafic and intermediate magmas, thus these estimates of degree of

717 fractional crystallisation from both MELTS and the least-squares modelling must be treated

718 with caution.

719   Lavas in the South Coast group have relatively high crystallinity compared with other

720 mafic and intermediate lavas (Table 3), with crystals that show the most zoning in BSE

721 imagery and major and trace element analyses (Fig. 6, 8), and feldspars that lie furthest from

722 the modelled equilibrium compositions (Fig. 9). These South Coast lavas are also observed to

723 contain significant proportions of plutonic lithic clasts (ranging from gabbros to syenites,

724 Roedder & Coombs, 1967; Harris et al., 1982; Harris, 1983; Webster & Rebbert, 2001).

725 These observations suggest that the range in compositions of feldspar and olivines found in

726 South Coast lavas is the result of incorporation of large amounts crystals from other sources,

727 as antecrysts or xenocrysts (Charlier et al., 2005). Potential sources of contaminant crystals

728 are oceanic crust (thus crystals are xenocrystic), plutonic bodies related to Ascension Island

729 magmatism (thus antecrysts), or from a mushy, not yet solid fractionated crystal residue (also

730 antecrysts, as in the other mafic to intermediate lavas, above). Few analyses of crystals from

731 the abundant lithic clasts exist, however feldspar compositions from gabbros overlap those

732 found in the mafic lavas (Harris, 1983) and isotopic data suggests a cogenetic origin for

733 gabbros and mafic lavas (Weis et al., 1987). Contrastingly, ocean crust feldspars define a

734 lower K_2O trend than alkaline-magmatism-sourced feldspars when plotted against An content

735 (Davis et al., 2007). No difference is seen in the feldspar and olivine compositions of the

736 South Coast lavas (Fig. 7 – 10), suggesting that incorporated crystals are antecrystic (and not

737 xenocrystic, see representative compositions of Mid-Atlantic Ridge feldspar crystals on Fig.

738 8b) in origin. No evidence is seen in crystal compositions or textures for mixing with a

739 chemically distinct magma, thus mechanical incorporation of antecrystic plutonic material

740 (e.g. Humphreys et al., 2009) is our favoured method by which these materials are included

741 within the South Coast lavas, on top of the 'background' accumulation of mushy antecrystic

742 material similar to the other mafic and intermediate lavas.

743   South coast lavas are the only samples studied here which show overgrowths on

744 feldspars (Fig. 6b), glomerocrystic textures (Fig. 5b) and increased crystallinity, suggestive of

745 higher degrees of antecryst incorporation. The relative importance of antecrysts in south coast

746 lavas could be due to these south coast magmas having a greater ability to erode these deep

747 mafic plutonic bodies upon ascent, or that that these deep mafic plutonic bodies are only

748 present in the source and ascent region of the crust through which the south coast lavas travel

749 prior to eruption. A magma's ability to mechanically disaggregate any lithic fragment is

750 dependent upon its enthalpy and composition (Glazner, 2007). The variations in whole rock

751 compositions between south coast lavas and other mafic lavas is not significant (Fig. 4), thus

752 only variations in temperature could change the magmas ability to erode and disaggregate the

753 plutonic lithic fragment. Modelled feldspar-melt temperatures are similar across the suite of

754 mafic lavas (Table 8) and so it seems unlikely that increased antecryst incorporation is due to

755 an increased ability of south coast magmas to erode plutonic lithic fragments. Instead, the

756 increased proportion of antecrysts in south coast lavas is suggested to reflect an increased

757 presence of mafic plutonic rocks at depth in this region. These plutonic rocks are anteliths,

758 related to Ascension Island generation and not oceanic crust plutonic rocks (Fig. 8b), and

759   highlight the lateral variability in plutonic or mushy regions within the Ascension Island

760   crust.

761

762   *Crustal control on the location of felsic eruptive centres*

763   Eruptions of felsic magma occurred from two main centres: the older central felsic complex,

764   and the younger eastern felsic complex with mafic magmas erupted around the peripheries of

765   these centres (Fig. 1; Jicha et al., 2013). In these regions, felsic magmas - erupted as lavas

766   and pyroclasts - are the dominant magma type. Spatial separation of mafic and felsic lavas

767   has been seen at other ocean islands (both active and extinct), and has been suggested to be a

768   result of crustal structure inhibiting the ascent of more dense mafic magmas in the felsic

769   complexes (e.g. Mahood & Hildreth, 1983; Druitt et al., 1995; Carracedo et al., 2007; Brenna

770   et al., 2015).

771   Active-source tomography reveals an area of elevated seismic velocities in the core of

772   the island, at 6.5 km depth beneath the felsic complexes (Evangelidis et al., 2004). This was

773   interpreted to represent a single crystallised magma body, supported by the presence of

774   plutonic lithic clasts in the erupted products (e.g. Roedder & Coombs, 1967; Harris, 1986;

775   Weis et al., 1987; Hobson, 2001; Webster & Rebbert, 2001). This central core of nested

776   plutonic rocks (of gabbroic through to granitic compositions – Roedder & Coombs, 1967)

777   under the felsic complexes could inhibit the ascent of almost all mafic magmas in these

778   regions.

779   The presence of plutonic rocks in ocean island crust has long been known to affect the

780   evolution of magmas prior to eruption—the volcanic islands of Terceira (Mungall & Martin,

781   1995) and Oki-Dōzen (Brenna et al., 2015), among others, have evidence for central felsic

782   complexes (both as plutonic rocks, and as storage regions for felsic volcanic eruptions) which

783   inhibit the eruption of mafic magmas. Ascension Island has a modelled growth rate of 0.4

784   km/Myr (Minshull et al., 2010), which is significantly lower even than post-shield Hawaii

785   (0.9 km/Myr, Minshull et al., 2010 and references therein) and dramatically lower than shield

786   stage Mauna Kea (8.6km/Myr, Minshull et al., 2010 and references therein). Therefore we

787   suggest that this 'filtering' of mafic magmas and spatial segregation of mafic and felsic

788   eruptive centres could be a result of low rates of magmatic flux. If magmatic flux is higher,

789   this could destabilise the central felsic systems, and mafic and felsic magmas would no

790   longer show such clear spatial separation, and mixing textures would be much more

791   dominant, such as those observed in Tenerife (Sliwinski et al., 2015) or Iceland (Carley et al.,

792   2011), where mafic and felsic magmas are still produced, but with less clear spatial

793   separation and increased role of partial melting of crustal material than that inferred at

794   Ascension.

795   We suggest that multiple plutonic bodies representative of multiple ephemeral magma

796   reservoirs, rather than a single magma body, are necessary to generate the range in

797   compositions seen on Ascension Island as there is no evidence from crystal compositions for

798   repeated use of a single magma storage region which is repeatedly rejuvenated (cf. Kahl et

799   al., 2013). This observation suggests the 'plutonic body' identified seismically (Evangelidis

800   et al., 2004) beneath Ascension is a series of smaller-volume, nested plutonic bodies which

801   cannot be resolved seismically from a single large body in the same dimensions (Bauer et al.,

802   2003).

803   The presence of plutonic lithic clasts in pyroclastic fall deposits on Ascension Island

804   (including some of the oldest fall units on the island, Hobson, 2001), combined with the

805   rhyolitic nature of the oldest-dated subaerial lava (Jicha et al., 2013), implies that the plutonic

806   complex was established well before the beginning of the subaerial phase of Ascension

807   Island's volcanic history. While the felsic plutonic and volcanic rocks share an apparently

808   common origin (with similar isotopic characteristics, Weis et al., 1987 and following the

809   same liquid line of descent, Harris et al., 1982) the timing of plutonic formation must pre-date

810   the earliest subaerial eruptions on the island (1094 ka; Jicha et al., 2013), and could relate to

811   the more voluminous submarine volcanism that began ~5 – 6 Myr ago (Minshull et al., 2010;

812   Paulick et al., 2010).

813

814   **The magmatic plumbing system**

815   Here we combine our new results with all previously published data to present a model for

816   the magmatic plumbing system underlying Ascension Island (Fig. 16) during the subaerial

817   phase of activity from ~1 Ma to present. The key features of the model are as follows:

818   1) A zone of melt extraction from which all Ascension Island volcanism is sourced, at

819   varying degrees of partial melt (Fig. 16; Paulick et al., 2010; Jicha et al., 2013). This

820   melt extraction zone is geochemically distinct from the mantle melting responsible for

821   the significantly larger volume submarine volcanism of Ascension which was active

822   from ~5-6 Ma to ~3 Ma (Minshull et al., 2010; Paulick et al., 2010).

823   2) Heterogeneity in the lower crust affects the ascent and incorporation of antecrysts in

824   basaltic melts. The variably over-thickened layer 3 (lower crust) presently underlying

825   Ascension Island (Klingelhöfer et al., 2001) likely formed during the large volume,

826   on-axis volcanism which built the submarine edifice (Minshull et al., 2010). We

827   suggest that the over-thickening of layer 3 (represented mainly by mafic plutonic

828   lithic clasts, not the nested felsic plutonic lithic clasts) is most significant underneath

829   the vents for the South Coast lavas (AI14-514, AI14-522). South Coast lavas contain

830   many crystals that are not in equilibrium with their whole rock compositions (Fig. 9),

831   suggesting that these magmas have mechanically incorporated large numbers of

832   antecrystic feldspar and olivine, shortly prior to eruption. This spatial heterogeneity in

833   deep mafic plutonic rocks is reflected in the proportions of antecrysts incorporated

834   during ascent of mafic magmas.

835 3) A central nested region of small discrete plutonic bodies of varying composition (of a

836   higher proportion of felsic bodies), which forces the majority of ascending mafic

837   magmas to stall and fractionate until they reach a level where their buoyancy has

838   increased enough to allow them to ascend further. This is supported by the felsic

839   plutonic lithic clasts within the Green Mountain scoria, erupted in the central felsic

840   complex, and by mechanically incorporated plutonic lithic fragments in many felsic

841   pyroclastic deposits (Fig. 16).

842 4) Felsic magma evolution occurs only in the lower crust at pressures greater than 170

843   MPa (Fig. 13). No evidence is seen for magmatic stalling (and subsequent eruption)

844   of felsic melts stored at pressures less than 170 MPa. The only modelled entrapment

845   pressures from melt inclusions from a zoned fall deposit on Ascension Island showed

846   that crystals grew in a storage region at 250 MPa (Chamberlain et al., 2016), with

847   melt inclusions having up to 4 wt.% H_2O. This is in agreement with modelled

848   entrapment pressures from felsic plutonic bodies being between 200 and 300 MPa (or

849   6.8 – 10.2 km, assuming a crustal density of 3000 kgm^{-3}; Webster & Rebbert, 2001).

850   The modelled high water concentrations of melts from which feldspars have grown

851   (Table 8) could support this storage and evolution within the lower crust (or Layer 3

852   of Klingelhöfer et al., 2001; Fig. 13, 16). Lower crustal storage means that any unrest

853   signals will be harder to resolve, and has implications for the methods implemented to

854   monitor future volcanic unrest on Ascension Island.

855 5) Magmas are erupted as discrete batches, with no evidence for long-lived storage, or

856   for crystal recycling between eruptions in a mushy or melt-dominant magma storage

857   region (cf. Kahl et al., 2013). Magma mixing is therefore not an eruptive trigger.

858   Instead, triggers could be internal (due to volatile over-pressure), or from external

859   tectonic changes, which again presents challenges for monitoring potential future

860   volcanic unrest at Ascension Island.

861   6) The magmas that fed explosive and effusive felsic eruptions exhibit differences in the

862   presence or absence of low pressure phases (Fig. 14) perhaps suggestive of variation

863   in the location of their storage regions and ascent rates, and warrants further

864   investigation. However, fractional crystallisation (with minor crystal entrainment) of

865   predominantly feldspars induced by stalling (at varying depths) in the nested (more

866   felsic) plutonic region, remains the dominant evolutionary process for all felsic

867   magmas, irrespective of the eruptive style.

868

869   **Implications for the generation of felsic magmas on ocean islands**

870   The petrogenetic processes responsible for the generation of felsic magmas in ocean island

871   volcanoes built on thin oceanic crust have long been debated. Many authors suggested that

872   felsic magma production at ocean island volcanoes could be a proxy for the initiation of

873   continental crust formation in the Archean (e.g., Gazel et al., 2014; Mancini et al., 2015).

874   While the low growth rates of Ascension Island (Minshull et al., 2010) negate its use in

875   understanding Archean felsic magma genesis, the dominance of fractional crystallisation in

876   the generation of felsic magmas, with little evidence for magma mixing, is unusual when

877   compared with other ocean island volcanoes (e.g., the Canary Islands and Iceland: e.g.

878   Borhson & Reid 1997; Caroff et al., 1999; Sverrisdottir, 2007; Carley et al., 2011; Longpré et

879   al., 2014).

880

881   *Open vs. closed system evolution*

882   The new data presented here suggests evolution of Ascension Island magmas is dominated by

883   simple crystal fractionation in a relatively closed system of short-lived discrete storage

884   regions, and supports conclusions of previous workers (Harris et al., 1982; Kar et al., 1998;

885   Webster & Rebbert, 2001; Jicha et al., 2013; Chamberlain et al., 2016). This is contrary to

886   many other ocean island volcanoes where open system processes such as magma mixing and

887   significant partial melting of oceanic crust contribute to the formation of evolved magmas,

888   and where there is less evidence for closed system fractional crystallisation (Bohrson & Reid

889   1995, 1997; Caroff et al., 1999; Carley et al., 2011; Weismaier et al., 2013; Longpré et al.,

890   2014; Sliwinski et al., 2015). The main factor controlling whether open or closed system

891   behaviour dominates could be the magmatic flux: it has been shown that increased magma

892   fluxes correspond to increased degrees of crustal assimilation and crystal entrainment at mid

893   ocean ridges (Michael & Cornell, 1998). Ascension Island has an order of magnitude slower

894   growth rate when compared with Hawaii (Sharp & Renne, 2005; Minshull et al., 2010), and

895   thus we infer a significantly lower magmatic flux, which led to the development of small-

896   scale, short-lived magma storage regions, and closed system evolution of felsic magmas.

897   Multiple volcanic centres also display evidence for relatively closed system evolution of

898   mafic magmas by extensive fractional crystallisation to produce alkaline felsic magmas (e.g.

899   Volcán Alcedo in the Galápagos [Geist et al., 1995], Terceira, São Miguel and Graciosa in

900   the Azores [Mungall & Martin, 1995; Larrea et al., 2014; Jeffrey et al., 2016], and the extinct

901   Oki-Dōzen volcano, Japan [Brenna et al., 2015]). These islands are all likely the result of low

902   magmatic production rates, and are likely not related to a deep-seated mantle hotspots

903   (Hildenbrand et al., 2014; Métrich et al., 2014). Fractional crystallisation always requires the

904   formation of a large volume of plutonic rocks as a by-product of extensive fractional

905   crystallisation. Erupted lithic fragments or surface exposures provide evidence for these

906 plutonic rocks (Mungall & Martin, 1995; Larrea et al., 2014; Brenna et al., 2015; Jeffrey et

907 al., 2016).

908

909 *Fractional crystallisation: the space problem*

910 Extensive fractional crystallisation of > 80% mafic melt to produce the felsic magmas seen

911 on small ocean islands such as Ascension Island and the Azores implies that significant

912 volumes of plutonic material remain in the crust. While eruptive volumes are unconstrained

913 at Ascension Island due to high erosion rates and dispersal over the ocean, the high degrees

914 of fractionation responsible for a single body of felsic magma evolution suggest that

915 significant volumes of plutonic rocks remain in the crust. Taking the evolution from NE Bay

916 scoria to Middleton's Ridge rhyolite as an example, in total the rhyolite represents only ~9%

917 of the original mass of basalt. If we assume a modest eruptive volume of 0.2 km^3 (compared

918 with the AD 1630 eruption from São Miguel which evacuated ~0.85 km^3 of magma [DRE,

919 Cole et al., 1995]), then ~2 km^3 of fractionated crystals, preserved as plutonic rocks, remain

920 in the crust. Erupted volumes and degree of fractionation vary between eruptions, yet as over

921 70 eruptions of felsic magma have occurred over the last 1 million years on Ascension

922 (Preece et al., 2016), then a minimum of ~140 km^3 of plutonic rocks may remain in the crust,

923 with no evidence for their rejuvenation preserved in any volcanic products on Ascension

924 Island. This could be viewed as a minimum volume, given the lack of constraints on eruptive

925 volumes, and the unknown number of magmatic (not necessarily eruptive) events. Evidence

926 for a central nested plutonic core (Evangelidis et al., 2004) and over-thickening of layer 3

927 (where magmatic evolution is interpreted to occur at Ascension Island, see above) has been

928 observed in seismic reflection surveys (Klingelhöfer et al., 2001). Evangelidis et al. (2004)

929 suggest that the central high velocity region, inferred to consist of plutonic rocks (of

930 unknown compositions), could have a volume approaching 7000 km^3. This appears large

931   compared to our minimum estimates (above), however small discrete bodies of plutonics of

932   varying composition would not be resolvable from the seismic reflection surveys, and

933   therefore this volume represents an area affected by plutonism, not necessarily the volumes of

934   individual plutonic bodies. Aside from over-thickening of layer 3 (Klingelhöfer et al., 2001),

935   it remains unclear how such large potential volumes of plutonic rocks are accommodated in

936   thin oceanic crust, yet their presence seems vital for the formation of evolved melts in low

937   magma flux ocean island volcanoes.

938

939   **CONCLUSIONS**

940   - There are no differences in whole rock or crystal compositions from the lavas erupted

941   in the same spatial regions of the island, suggesting that in the last 1 Myr the

942   processes controlling mafic melt production and eruption have remained constant,

943   even if source region composition and degree of partial melting have changed (cf.

944   Jicha et al., 2013).

945   - Spatial variation in crystallinity and in the composition and origin of crystals between

946   mafic eruptive centres highlights heterogeneity in the lower crust under Ascension

947   Island. The mafic magmas which erupted along the South Coast region, as well as the

948   Green Mountain scoria sample in the felsic complexes incorporated higher volumes of

949   antecrysts during ascent, consistent with the observation of increased numbers of

950   coherent plutonic lithic fragments in these lava flows.

951   - Felsic melt evolution at Ascension Island is dominantly controlled by crystal

952   fractionation of ternary feldspar with minor fayalite or sodic clinopyroxene,

953   dependent upon ascent rate and oxidation state of the magma, with isotopic evidence

954   of minor crustal assimilation of seawater-altered crustal material (Kar et al., 1998).

955   There is no evidence for magma mixing in any of the eruptive deposits studied here,

956   indicating that while a wide range of magma compositions are erupted across a ~12

957   km diameter island, they do not encounter other melts during their transport through

958   the crust. Magmatic evolution occurs in small, short-lived, isolated magma storage

959   regions in the lower crust. Antecrysts do not show reaction rims, and therefore their

960   incorporation is purely mechanical and occurred late (during ascent).

961 • Alkali feldspar-melt hygrometry reveals high water concentrations of up to 8 wt.%

962   H_2O in the more-evolved magmas. These high H_2O concentrations, combined with

963   the lack of evidence for an external trigger in the crystal chemistry suggests that

964   internal over-pressure from high degrees of fractional crystallisation concentrating

965   H_2O in the liquid phase is a likely eruptive trigger for explosive eruptions on

966   Ascension Island.

967 • Felsic magmas are almost entirely erupted in the central and eastern areas of

968   Ascension Island implying a spatial control on the evolution of felsic melts. We infer

969   that the presence of significant volumes of plutonic bodies at depth inhibits magma

970   ascent in these regions, and allow magmas to evolve and incorporate antecrysts.

971   While the origin and nature of these plutonic bodies is not yet known, they must pre-

972   date the subaerial stage of Ascension Island volcanism. The presence of plutonic

973   rocks as abundant lithic clasts in the central and eastern regions highlights the

974   importance of heterogeneous crustal structure in the evolution of magmas in thin

975   young oceanic crust at Ascension Island.

976

993

994 **REFERENCES**

995 Ablay, G. J., Carroll, M. R., Palmer, M. R., Martí, J., & Sparks, R. S. J. (1998). Basanite–

996   phonolite lineages of the Teide–Pico Viejo volcanic complex, Tenerife, Canary

997   Islands. *Journal of Petrology*, *39*(5), 905-936.

998 Allan, A. S., Wilson, C. J., Millet, M. A., & Wysoczanski, R. J. (2012). The invisible hand:

999   Tectonic triggering and modulation of a rhyolitic supereruption. *Geology, 40(6),* 563-

1000   566.

1001 Almeev, R., Holtz, F., Koepke, J., Haase, K., & Devey, C. (2008). Depths of partial

1002   crystallization of H_2O-bearing MORB: phase equilibria simulations of basalts at the

1003   MAR near Ascension Island (7–11 S). *Journal of Petrology*, *49*(1), 25-45.

1004 Arth, J. G. (1976). Behavior of trace elements during magmatic processes: a summary of

1005   theoretical models and their applications. *J. Res. US Geol. Surv.;(United States)*, *4*(1).

1006 Ashwal, L., Torsvik, T., Horváth, P., Harris, C., Webb, S., Werner, S., & Corfu, F. (2016). A

1007   Mantle-derived Origin for Mauritian Trachytes. *Journal of Petrology*, *57(*9*)*, 1645-

1008   1676

1009 Bacon, C. R. & Hirschmann, M. M. (1988). Mg/Mn partitioning as a test for equilibrium

1010   between coexisting Fe^Ti oxides. *American Mineralogist 73,* 57-61

1011 Bauer, K., Trumbull, R. B., & Vietor, T. (2003). Geophysical images and a crustal model of

1012   intrusive structures beneath the Messum ring complex, Namibia. *Earth and Planetary*

1013   *Science Letters*, *216*(1-2), 65-80.

1014 Bohrson, W. A., & Reid, M. R. (1995). Petrogenesis of alkaline basalts from Socorro Island,

1015   Mexico: Trace element evidence for contamination of ocean island basalt in the

1016   shallow ocean crust. *Journal of Geophysical Research: Solid Earth*, *100*(B12), 24555-

1017   24576.

1018 Bohrson, W. A., & Reid, M. R. (1997). Genesis of silicic peralkaline volcanic rocks in an

1019   ocean island setting by crustal melting and open-system processes: Socorro Island,

1020   Mexico. *Journal of Petrology*, *38*(9), 1137-1166.

1021 Bohrson, W. A., Reid, M. R., Grunder, A. L., Heizler, M. T., Harrison, T. M., & Lee, J.

1022   (1996). Prolonged history of silicic peralkaline volcanism in the eastern Pacific

1023   Ocean. *Journal of Geophysical Research: Solid Earth*, *101*(B5), 11457-11474.

1024 Bottinga, Y., & Weill, D. F. (1970). Densities of liquid silicate systems calculated from

1025   partial molar volumes of oxide components. *American Journal of Science, 269(2)*,

1026   169-182.

1027 Brenna, M., Nakada, S., Miura, D., Toshida, K., Ito, H., Hokanishi, N., & Nakai, S. I. (2015).

1028   A trachyte–syenite core within a basaltic nest: filtering of primitive injections by a

1029   multi-stage magma plumbing system (Oki-Dōzen, south-west Japan). *Contributions to*

1030   *Mineralogy and Petrology*, *170*(2), 1-21.

1031   Burke, K. C., & Wilson, J. T. (1976). Hot spots on the Earth's surface. *Scientific American,*

1032   *235*(2), 46-59.

1033   Caricchi, L., Sheldrake, T. E., & Blundy, J. (2018). Modulation of magmatic processes by

1034   CO2 flushing. *Earth and Planetary Science Letters, 491,* 160-171.

1035   Carley, T. L., Miller, C. F., Wooden, J. L., Bindeman, I. N., & Barth, A. P. (2011). Zircon

1036   from historic eruptions in Iceland: reconstructing storage and evolution of silicic

1037   magmas. *Mineralogy and Petrology*, *102*(1-4), 135-161.

1038   Caroff, M., Guillou, H., Lamiaux, M., Maury, R. C., Guille, G., & Cotten, J. (1999).

1039   Assimilation of ocean crust by hawaiitic and mugearitic magmas: an example from

1040   Eiao (Marquesas). *Lithos*, *46*(2), 235-258.

1041   Carracedo, J.C., Badiola, E.R., Guillou, H., Paterne, M., Scaillet, S., Torrado, F.P., Paris, R.,

1042   Fra-Paleo, U. & Hansen, A., (2007). Eruptive and structural history of Teide Volcano

1043   and rift zones of Tenerife, Canary Islands. *Geological Society of America*

1044   *Bulletin*, *119*(9-10), 1027-1051.

1045   Chamberlain, K. J., Barclay, J., Preece, K., Brown, R. J., & Davidson, J. P. (2016). Origin

1046   and evolution of silicic magmas at ocean islands: Perspectives from a zoned fall

1047   deposit on Ascension Island, South Atlantic. *Journal of Volcanology and Geothermal*

1048   *Research, 327,* 349-360.

1049   Charlier, B. L. A., Wilson, C. J. N., Lowenstern, J. B., Blake, S., Van Calsteren, P. W., &

1050   Davidson, J. P. (2005). Magma generation at a large, hyperactive silicic volcano

1051   (Taupo, New Zealand) revealed by U–Th and U–Pb systematics in zircons. *Journal of*

1052   *Petrology*, *46*(1), 3-32.

1053   Charlier, B., Namur, O., & Grove, T. L. (2013). Compositional and kinetic controls on liquid

1054   immiscibility in ferrobasalt–rhyolite volcanic and plutonic series. *Geochimica et*

1055   *Cosmochimica Acta*, *113*, 79-93.

1056   Cole, P. D., Queiroz, G., Wallenstein, N., Gaspar, J. L., Duncan, A. M., & Guest, J. E.

1057   (1995). An historic subplinian/phreatomagmatic eruption: the 1630 AD eruption of

1058   Furnas volcano, Saõ Miguel, Azores. *Journal of Volcanology and Geothermal*

1059   *Research*, *69*(1), 117-135.

1060   Coogan, L.A., Kempton, P. D., Saunders, A. D., Norry, M. J. (2000): Melt aggregation within

1061   the crust beneath the Mid-Atlantic Ridge: evidence from plagioclase and

1062   clinopyroxene major and trace element compositions. *Earth and Planetary Science*

1063   *Letters*, *176*(2), 245-257.

1064   Coombs, D. W. (1963). Trends and affinities of basaltic magmas and pyroxenes as illustrated

1065   on the diopside-olivine-silica diagram: in Miscellaneous papers—International

1066   Mineralogical Association Third General Meeting, Mineral. Soc. Amer., Spec. Pap.,

1067   Vol. 1, p. 227-250.

1068   Daly, R. A. (1925, June). The geology of Ascension Island. In *Proceedings of the American*

1069   *Academy of Arts and Sciences* (Vol. 60, No. 1, pp. 3-80). American Academy of Arts

1070   & Sciences.

1071   Davidson J. P., Kar A. & Weaver B. L. (1997). The origin of extreme isotope signatures

1072   among differentiated rocks from Ascension Island. *Geological Society of America,*

1073   *Abstracts with Programs 29*, A-89.

1074   Davis, A. S., Clague, D. A., & Paduan, J. B. (2007). Diverse origins of xenoliths from

1075   seamounts at the continental margin, offshore central California. *Journal of*

1076   *Petrology*, *48*(5), 829-852.

1077   Di Matteo, V., Carroll, M. R., Behrens, H., Vetere, F., & Brooker, R. A. (2004). Water

1078   solubility in trachytic melts. *Chemical Geology*, *213*(1-3), 187-196.

1079 Druitt, T. H., Brenchley, P. J., Gökten, Y. E., & Francaviglia, V. (1995). Late Quaternary

1080   rhyolitic eruptions from the Acigöl Complex, central Turkey. *Journal of the*

1081   *Geological Society*, *152*(4), 655-667.

1082 Eichelberger, J. C. (1995). Silicic volcanism: ascent of viscous magmas from crustal

1083   reservoirs. *Annual Review of Earth and Planetary Sciences*, *23*(1), 41-63.

1084 Evangelidis, C. P., Minshull, T. A., & Henstock, T. J. (2004). Three-dimensional crustal

1085   structure of Ascension Island from active source seismic tomography. *Geophysical*

1086   *Journal International*, *159*(1), 311-325.

1087 Ewart, A., & Griffin, W. L. (1994). Application of proton-microprobe data to trace-element

1088   partitioning in volcanic rocks. *Chemical Geology*, *117*(1-4), 251-284.

1089 Fowler, S. J., & Spera, F. J. (2010). A metamodel for crustal magmatism: phase equilibria of

1090   giant ignimbrites. *Journal of Petrology, 51*(9), 1783-1830.

1091 Gazel, E., Hayes, J. L., Kelemen, P. B., Everson, E. D., Holbrook, W. S., & Vance, E. (2014,

1092   December). Generation of continental crust in intra-oceanic arcs. In *AGU Fall*

1093   *Meeting Abstracts* (Vol. 1, p. 4845).

1094 Geist, D. J., White, W. M., & McBirney, A. R. (1988). Plume-asthenosphere mixing beneath

1095   the Galapagos archipelago. *Nature*, *333*(6174), 657.

1096 Geist, D., Howard, K. A., & Larson, P. (1995). The generation of oceanic rhyolites by crystal

1097   fractionation: the basalt-rhyolite association at Volcan Alcedo, Galapagos

1098   Archipelago. *Journal of Petrology*, *36*(4), 965-982.

1099 Ghiorso, M. S., & Evans, B. W. (2008). Thermodynamics of rhombohedral oxide solid

1100   solutions and a revision of the Fe-Ti two-oxide geothermometer and oxygen-barometer.

1101   *American Journal of Science*, *308*(9), 957-1039.

1102   Giordano, D., Romano, C., Dingwell, D. B., Poe, B., & Behrens, H. (2004). The combined

1103   effects of water and fluorine on the viscosity of silicic magmas. *Geochimica et*

1104   *Cosmochimica Acta*, *68*(24), 5159-5168.

1105   Glazner, A. F. (2007). Thermal limitations on incorporation of wall rock into

1106   magma. *Geology*, *35*(4), 319-322.

1107   Goldich, S. S., Ingamells, C. O., Suhr, N. H. & Anderson, D. H. (1967). Analyses of silicate

1108   rock and mineral standards. *Canadian Journal of Earth Sciences* **4**, 747-755.

1109   Gualda, G. A., & Ghiorso, M. S. (2015). MELTS_Excel: A Microsoft Excel‐based MELTS

1110   interface for research and teaching of magma properties and evolution. *Geochemistry,*

1111   *Geophysics, Geosystems*, *16*(1), 315-324.

1112   Gualda, G. A., Ghiorso, M. S., Lemons, R. V., & Carley, T. L. (2012). Rhyolite-MELTS: a

1113   modified calibration of MELTS optimized for silica-rich, fluid-bearing magmatic

1114   systems. *Journal of Petrology, 53*(5), 875-890.

1115   Harpp, K. S., & White, W. M. (2001). Tracing a mantle plume: Isotopic and trace element

1116   variations of Galápagos seamounts. *Geochemistry, Geophysics, Geosystems*, *2*(6).

1117   Harris, C. (1983). The petrology of lavas and associated plutonic inclusions of Ascension

1118   Island. *Journal of Petrology*, *24*(4), 424-470.

1119   Harris, C. (1986). A quantitative study of magmatic inclusions in the plutonic ejecta of

1120   Ascension Island. *Journal of Petrology*, *27*(1), 251-276.

1121   Harris, C., Bell, J. D., & Atkins, F. B. (1982). Isotopic composition of lead and strontium in

1122   lavas and coarse-grained blocks from Ascension Island, South Atlantic. *Earth and*

1123   *Planetary Science Letters*, *60*(1), 79-85.

1124   Hildenbrand, A., Weis, D., Madureira, P., & Marques, F. O. (2014). Recent plate re-

1125   organization at the Azores Triple Junction: Evidence from combined geochemical and

1126   geochronological data on Faial, S. Jorge and Terceira volcanic islands. *Lithos*, *210*,

1127   27-39.

1128   Hobson, K.E. (2001). The pyroclastic deposits and eruption history of Ascension Island: a

1129   palaeomagnetic and volcanological study. *Doctoral dissertation, University of*

1130   *Oxford*.

1131   Humphreys, M. C., Christopher, T., & Hards, V. (2009). Microlite transfer by disaggregation

1132   of mafic inclusions following magma mixing at Soufrière Hills volcano,

1133   Montserrat. *Contributions to Mineralogy and Petrology*, *157*(5), 609-624.

1134 Ingamells, C. O. (1980). Analysed minerals for electron microprobe standards. *Geostandards*

1135   *Newsletter* **2**, 115.

1136 Jarosewich, E., Nelen, J. A. & Norberg, J. A. (1980). Reference samples for electron

1137   microprobe analysis. *Geostandards Newsletter* **4,** 43-47.

1138 Jeffery, A. J., Gertisser, R., O'Driscoll, B., Pacheco, J. M., Whitley, S., Pimentel, A., & Self, S.

1139   (2016). Temporal evolution of a post-caldera, mildly peralkaline magmatic system:

1140   Furnas volcano, São Miguel, Azores. *Contributions to Mineralogy and*

1141   *Petrology*, *171*(5), 1-24

1142 Jicha, B. R., Singer, B. S., & Valentine, M. J. (2013). 40Ar/39Ar Geochronology of Subaerial

1143   Ascension Island and a Re-evaluation of the Temporal Progression of Basaltic to

1144   Rhyolitic Volcanism. *Journal of Petrology*, *54*(12), 2581-2596.

1145 Jochum, K. P., Weis, U., Stoll, B., Kuzmin, D., Yang, Q., Raczek, I., Jacob, D.E., Stracke, A.,

1146   Birbaum, K., Frick, D.A. & Günther, D. (2011). Determination of reference values for

1147   NIST SRM 610–617 glasses following ISO guidelines. *Geostandards and*

1148   *Geoanalytical Research*, *35*(4), 397-429.

1149   Jochum, K. P., Weis, U., Schwager, B., Stoll, B., Wilson, S. A., Haug, G. H., Andreae, M. O.

1150   & Enzweiler, J. (2016). Reference values following ISO guidelines for frequently

1151   requested rock reference materials. *Geostandards and Geoanalytical Research*, *40*(3),

1152   333-350.

1153   Kahl, M., Chakraborty, S., Costa, F., Pompilio, M., Liuzzo, M., & Viccaro, M. (2013).

1154   Compositionally zoned crystals and real-time degassing data reveal changes in

1155   magma transfer dynamics during the 2006 summit eruptive episodes of Mt.

1156   Etna. *Bulletin of Volcanology*, *75*(2), 1-14

1157   Kar, A. (1997). A comprehensive geological, geochemical, and petrogenetic study of hotspot-

1158   related oceanic basalt–rhyolite series rocks from Ascension Island, South Atlantic

1159   Ocean. Norman: University of Oklahoma. p. 260. Unpublished Ph.D. dissertation.

1160   Kar, A., Weaver, B., Davidson, J., & Colucci, M. (1998). Origin of differentiated volcanic

1161   and plutonic rocks from Ascension Island, South Atlantic Ocean. *Journal of*

1162   *Petrology*, *39*(5), 1009-1024.

1163   Klingelhöfer, F., Minshull, T. A., Blackman, D. K., Harben, P., & Childers, V. (2001).

1164   Crustal structure of Ascension Island from wide-angle seismic data: implications for

1165   the formation of near-ridge volcanic islands. *Earth and Planetary Science Letters*,

1166   *190*(1), 41-56

1167   Klügel, A. Hansteen, T. H. & Galipp, K. (2005). Magma storage and underplating beneath

1168   Cumbre Vieja volcano, La Palma (Canary Islands). *Earth and Planetary Science*

1169   *Letters* **236**, 211-226.

1170   Koppers, A. A., & Staudigel, H. (2005). Asynchronous bends in Pacific seamount trails: a

1171   case for extensional volcanism? *Science*, *307*(5711), 904-907.

1172   Kuehn, S. C., Froese, D. G., Pearce, N. J., & Foit, F. F. (2009, December). ID3506, a new/old

1173   Lipari obsidian standard for characterization of natural glasses and for

1174   tephrochronology. In *AGU Fall Meeting Abstracts*.

1175   Kuritani, T., Yokoyama, T., Kitagawa, H., Kobayashi, K., & Nakamura, E. (2011).

1176   Geochemical evolution of historical lavas from Askja Volcano, Iceland: Implications

1177   for mechanisms and timescales of magmatic differentiation. *Geochimica et*

1178   *Cosmochimica Acta*, *75*(2), 570-587.

1179   Larrea, P., Galé, C., Ubide, T., Widom, E., Lago, M., & França, Z. (2014). Magmatic

1180   Evolution of Graciosa (Azores, Portugal). *Journal of Petrology*, *55*(11), 2125-2154.

1181   Lemarchand, F., Villemant, B., & Calas, G. (1987). Trace element distribution coefficients in

1182   alkaline series. *Geochimica et Cosmochimica Acta*, *51*(5), 1071-1081.

1183   Longpré, M. A., Klügel, A., Diehl, A., & Stix, J. (2014). Mixing in mantle magma reservoirs

1184   prior to and during the 2011–2012 eruption at El Hierro, Canary

1185   Islands. *Geology*, *42*(4), 315-318.

1186   Luhr, J. F., & Carmichael, I. S. (1990). Petrological monitoring of cyclical eruptive activity at

1187   Volcan Colima, Mexico. *Journal of Volcanology and Geothermal Research*, *42*(3),

1188   235-260.

1189   Mahood, G. A., & Stimac, J. A. (1990). Trace-element partitioning in pantellerites and

1190   trachytes. *Geochimica et Cosmochimica Acta*, *54*(8), 2257-2276.

1191   Mahood, G., & Hildreth, W. (1983). Large partition coefficients for trace elements in high-

1192   silica rhyolites. *Geochimica et Cosmochimica Acta*, *47*(1), 11-30.

1193   Mancini, A., Mattsson, H. B., & Bachmann, O. (2015). Origin of the compositional diversity

1194   in the basalt-to-dacite series erupted along the Heiðarsporður ridge, NE Iceland.

1195   *Journal of Volcanology and Geothermal Research*, *301*, 116-127.

1196   Markl, G., Marks, M. A., & Frost, B. R. (2010). On the controls of oxygen fugacity in the

1197   generation and crystallization of peralkaline melts. *Journal of Petrology*, *51*(9), 1831-

1198   1847.

1199   Meade, F. C., Troll, V. R., Ellam, R. M., Freda, C., Font, L., Donaldson, C. H., &

1200   Klonowska, I. (2014). Bimodal magmatism produced by progressively inhibited

1201   crustal assimilation. *Nature Communications*, *5,* 4199.

1202   Métrich, N., Zanon, V., Créon, L., Hildenbrand, A., Moreira, M., & Marques, F. O. (2014). Is

1203   the 'Azores hotspot'a wetspot? Insights from the geochemistry of fluid and melt

1204   inclusions in olivine of Pico basalts. *Journal of Petrology*, *55*(2), 377-393.

1205   Michael, P. J., & Cornell, W. C. (1998). Influence of spreading rate and magma supply on

1206   crystallization and assimilation beneath mid-ocean ridges: Evidence from chlorine

1207   and major element chemistry of mid-ocean ridge basalts. *Journal of Geophysical*

1208   *Research: Solid Earth, 103(*B8), 18325-18356.

1209   Minshull, T. A., Ishizuka, O., & Garcia-Castellanos, D. (2010). Long-term growth and

1210   subsidence of Ascension Island: Constraints on the rheology of young oceanic

1211   lithosphere. *Geophysical Research Letters*, *37*(23).

1212   Mollo, S., Masotta, M., Forni, F., Bachmann, O., De Astis, G., Moore, G., & Scarlato, P.

1213   (2015). A K-feldspar–liquid hygrometer specific to alkaline differentiated

1214   magmas. *Chemical Geology*, *392*, 1-8.

1215   Montelli, R., Nolet, G., Dahlen, F. A., Masters, G., Engdahl, E. R., & Hung, S. H. (2004).

1216   Finite-frequency tomography reveals a variety of plumes in the

1217   mantle. *Science*, *303*(5656), 338-343

1218   Montelli, R., Nolet, G., Dahlen, F. A., & Masters, G. (2006). A catalogue of deep mantle

1219   plumes: New results from finite‐frequency tomography. *Geochemistry, Geophysics,*

1220   *Geosystems*, *7*(11).

1221   Mungall, J. E., & Martin, R. F. (1995). Petrogenesis of basalt-comendite and basalt-

1222   pantellerite suites, Terceira, Azores, and some implications for the origin of ocean-

1223   island rhyolites. *Contributions to Mineralogy and Petrology*, *119*(1), 43-55.

1224   Nash, W. P., & Crecraft, H. R. (1985). Partition coefficients for trace elements in silicic

1225   magmas. *Geochimica et Cosmochimica Acta*, *49*(11), 2309-2322

1226   Niu, Y., Wilson, M., Humphreys, E. R., & O'hara, M. J. (2011). The origin of intra-plate

1227   ocean island basalts (OIB): the lid effect and its geodynamic implications. *Journal of*

1228   *Petrology, 52*(7-8), 1443-1468.

1229   Nielson, D. L., & Sibbett, B. S. (1996). Geology of Ascension Island, South Atlantic Ocean.

1230   *Geothermics*, *25*(4), 427-448.

1231   Palme, H., & O'Neill, H. S. C. (2003). Cosmochemical estimates of mantle

1232   composition. *Treatise on Geochemistry*, *2*, 568.

1233   Panjasawatwong, Y., Danyushevsky, L. V., Crawford, A. J., & Harris, K. L. (1995). An

1234   experimental study of the effects of melt composition on plagioclase-melt equilibria at

1235   5 and 10 kbar: implications for the origin of magmatic high-An

1236   plagioclase. *Contributions to Mineralogy and Petrology*, *118*(4), 420-432.

1237   Papale, P., Neri, A., & Macedonio, G. (1998). The role of magma composition and water

1238   content in explosive eruptions: 1. Conduit ascent dynamics. *Journal of Volcanology*

1239   *and Geothermal Research*, *87*(1-4), 75-93.

1240   Paulick, H., Münker, C., & Schuth, S. (2010). The influence of small-scale mantle

1241   heterogeneities on Mid-Ocean Ridge volcanism: evidence from the southern Mid-

1242   Atlantic Ridge (7 30′ S to 11 30′ S) and Ascension Island. *Earth and Planetary*

1243   *Science Letters*, *296*(3), 299-310.

1244   Pearce, J. A., & Norry, M. J. (1979). Petrogenetic implications of Ti, Zr, Y, and Nb variations

1245   in volcanic rocks. *Contributions to Mineralogy and Petrology*, *69*(1), 33-47.

1246   Petrelli, M., Poli, G., Perugini, D., & Peccerillo, A. (2005). PetroGraph: A new software to

1247   visualize, model, and present geochemical data in igneous petrology. *Geochemistry,*

1248   *Geophysics, Geosystems*, *6*(7).

1249   Preece, K., Mark, D. F., Barclay, J., Cohen, B. E., Chamberlain, K. J., Jowitt, C., Vye-Brown,

1250   C., Brown, R. J. (2018). Bridging the gap: ^{40}Ar/^{39}Ar dating of volcanic eruptions from

1251   the 'Age of Discovery'. *Geology, 46*(12), 1035-1038.

1252   Preece, K., Barclay, J., Brown, R., Mark, D. F., Chamberlain, K, Cohen, B. E., Vye-Brown,

1253   C. (2016) A 1 million year eruption history of Ascension Island: insights from

1254   stratigraphy and ^{40}Ar/^{39}Ar dating. Cities on Volcanoes 9, Puerto Varas, Chile, Nov,

1255   2016

1256   Price, R. C., Gamble, J. A., Smith, I. E., Maas, R., Waight, T., Stewart, R. B., & Woodhead,

1257   J. (2012). The anatomy of an Andesite volcano: a time–stratigraphic study of andesite

1258   petrogenesis and crustal evolution at Ruapehu Volcano, New Zealand. *Journal of*

1259   *Petrology*, *53*(10), 2139-2189.

1260   Putirka, K. D. (2008). Thermometers and barometers for volcanic systems. *Reviews in*

1261   *Mineralogy and Geochemistry*, *69*(1), 61-120.

1262   Roedder, E., & Coombs, D. S. (1967). Immiscibility in Granitic Melts, Indicated by Fluid

1263   Inclusions in Ejected Granitic Blocks from Ascension Island. *Journal of*

1264   *Petrology*, *8*(3), 417-451.

1265   Rooney, T. O., Hart, W. K., Hall, C. M., Ayalew, D., Ghiorso, M. S., Hidalgo, P., & Yirgu,

1266   G. (2012). Peralkaline magma evolution and the tephra record in the Ethiopian Rift.

1267   *Contributions to Mineralogy and Petrology, 164*(3), 407-426.

1268   Rollinson, H. R. (1993). *Using geochemical data: evaluation, presentation, interpretation*.

1269   Routledge.

1270   Scoates, J. S. (2000). The plagioclase–magma density paradox re-examined and the

1271   crystallization of Proterozoic anorthosites. *Journal of Petrology, 41(5)*, 627-649.

1272   Sharp, W. D., & Renne, P. R. (2005). The 40Ar/39Ar dating of core recovered by the Hawaii

1273   Scientific Drilling Project (phase 2), Hilo, Hawaii. *Geochemistry, Geophysics,*

1274   *Geosystems, 6*(4).

1275   Sliwinski, J. T., Bachmann, O., Ellis, B. S., Dávila-Harris, P., Nelson, B. K., & Dufek, J.

1276   (2015). Eruption of Shallow Crystal Cumulates during Explosive Phonolitic Eruptions

1277   on Tenerife, Canary Islands. *Journal of Petrology, 56*(11), 2173-2194.

1278   Sparks, R. S. J., & Sigurdsson, H. (1987). The 1875 eruption of Askja volcano, Iceland:

1279   combined fractional crystallization and selective contamination in the generation of

1280   rhyolitic magma. *Mineralogical Magazine, 51*(360), 183-202.

1281   Stock, M. J., Humphreys, M. C., Smith, V. C., Isaia, R., & Pyle, D. M. (2016). Late-stage

1282   volatile saturation as a potential trigger for explosive volcanic eruptions. *Nature*

1283   *Geoscience, 9(3),* 249.

1284   Stormer, J. C., & Nicholls, J. (1978). XLFRAC: a program for the interactive testing of

1285   magmatic differentiation models. *Computers & Geosciences, 4*(2), 143-159.

1286   Sverrisdottir, G. (2007). Hybrid magma generation preceding Plinian silicic eruptions at

1287   Hekla, Iceland: evidence from mineralogy and chemistry of two zoned deposits.

1288   *Geological Magazine, 144*(04), 643-659.

1289   Troll, V. R., & Schmincke, H. U. (2002). Magma mixing and crustal recycling recorded in

1290   ternary feldspar from compositionally zoned peralkaline ignimbrite 'A', Gran

1291   Canaria, Canary Islands. *Journal of Petrology, 43*(2), 243-270.

1292   Watson, E. B., & Green, T. H. (1981). Apatite/liquid partition coefficients for the rare earth

1293   elements and strontium. *Earth and Planetary Science Letters, 56*, 405-421.

1294   Weaver, B. L., Wood, D. A., Tarney, J., & Joron, J. L. (1987). Geochemistry of ocean island

1295   basalts from the south Atlantic: Ascension, Bouvet, St. Helena, Gough and Tristan da

1296   Cunha. *Geological Society, London, Special Publications, 30*(1), 253-267.

1297 Weaver, B., Kar, A., Davidson, J., & Colucci, M. (1996). Geochemical characteristics of

1298   volcanic rocks from Ascension Island, South Atlantic Ocean. *Geothermics*, *25*(4),

1299   449-470.

1300 Webster, J. D., & Rebbert, C. R. (2001). The geochemical signature of fluid-saturated magma

1301   determined from silicate melt inclusions in Ascension Island granite xenoliths.

1302   *Geochimica et Cosmochimica Acta*, *65*(1), 123-136.

1303 Weis, D., Demaiffe, D., Cauet, S., & Javoy, M. (1987). Sr, Nd, O and H isotopic ratios in

1304   Ascension Island lavas and plutonic inclusions; cogenetic origin. *Earth and Planetary*

1305   *Science Letters*, *82*(3), 255-268.

1306 Wiesmaier, S., Troll, V. R., Wolff, J. A., & Carracedo, J. C. (2013). Open-system processes

1307   in the differentiation of mafic magma in the Teide–Pico Viejo succession, Tenerife.

1308   *Journal of the Geological Society*, *170*(3), 557-570.

1309 White, J. C., Holt, G. S., Parker, D. F., & Ren, M. (2003). Trace-element partitioning

1310   between alkali feldspar and peralkalic quartz trachyte to rhyolite magma. Part I:

1311   Systematics of trace-element partitioning. *American Mineralogist*, *88*(2-3), 316-329.

1312 White, J. C., Parker, D. F., & Ren, M. (2009). The origin of trachyte and pantellerite from

1313   Pantelleria, Italy: insights from major element, trace element, and thermodynamic

1314   modelling. *Journal of Volcanology and Geothermal Research*, *179*(1), 33-55.

1315 Zhao, D. (2004). Global tomographic images of mantle plumes and subducting slabs: insight

1316   into deep Earth dynamics. *Physics of the Earth and Planetary Interiors*, *146*(1), 3-34.

FIGURE CAPTIONS

1318 Figure 1: Geological map of Ascension Island, located 90 km from the Mid Atlantic Ridge

1319 and between the Ascension Fracture Zone (AFZ) and Boca Verde Fracture Zone

1320 (BVFZ; inset), adapted from Weaver et al. (1995), Paulick et al. (2010) & Chamberlain

1321 et al. (2016). Sample locations indicated by triangles, diamonds and pentagons;

1322 eruptive centres identified in grey font. Surface expressions of known faults outlined in

1323 red. Major lava flow boundaries are indicated with black lines in the mafic lava flows.

1324 Figure 2: (a) Radiogenic isotope variations in Ascension Island lavas (subaerial unless

1325 otherwise stated); (b) Trace HFSE variation with major element variations; (c) Adapted

1326 from Jicha et al., 2013, trace element variation in Ascension lavas, showing the

1327 variation due to source heterogeneity, differentiation, and Fe-Ti oxide controlled

1328 fractionation paths; (d) variation in ^{143}Nd/^{144}Nd with degree of evolution (MgO). All

1329 data presented is a combination of Weaver et al. (1995, grey diamonds), Kar et al.

1330 (1998, orange diamonds), Paulick et al. (2010, blue squares) and Jicha et al. (2013,

1331 crosses).

1332 Figure 3: (a) Whole rock compositions of selected samples compared with all known

1333 Ascension Island whole rock data in grey field- (data from Weaver et al., 1996, Kar et

1334 al., 1998, Jicha et al., 2013). Diagram adapted from LeMaitre et al. (1989). (b)

1335 Primitive mantle (Palme & O'Neill, 2003) normalised trace element ranges for mafic-

1336 intermediate lavas (purple), scoria samples (orange), pumice samples (yellow) and

1337 felsic lava samples (blue).

1338 Figure 4: Whole rock variation in major and trace elements for all studied samples of

1339 Ascension Island mafic-intermediate lavas (purple triangles), felsic lavas (blue

1340 pentagons) and pyroclastics both pumiceous (yellow diamonds) and scoriaceous

1341 (orange diamonds). Grey fields represent the full range of compositions found at

1342 Ascension from Weaver et al. (1995). For full data set, see Electronic Appendix 2.

1343 Figure 5: Photomicrographs of Ascension lava samples. (a, b): Young South Coast lava

1344 sample showing a glomerocryst of feldspar and olivine; (c, d): Young Sisters lava

1345 sample showing euhedral plagioclase feldspar in a microcrystalline matrix; (e, f):

1346 Cricket Valley lava with sodic feldspars and minor aegirine-augite in a microcrystalline

1347 groundmass; (g): Letterbox felsic lava with large ternary feldspar phenocrysts in a

1348 microcrystalline groundmass; (h): Ariane lava flow with ternary feldspars and aegirine-

1349 augite in a microcrystalline groundmass. Images (a, c, e, g) in plane-polarised light;

1350 images (b, d, f, h) in cross-polarised light. Sample numbers relate to those listed in

1351 Table 1 and numbers in square brackets show whole rock SiO_2 concentrations.

1352 Figure 6: Back Scattered Electron (BSE) images of Ascension Island lavas. Sample numbers

1353 relate to those listed in Table 1 and numbers in square brackets show whole rock SiO_2

1354 concentrations. Features labelled in red refer to A: Reverse-zoned feldspar; B:

1355 Normally-zoned olivine; C: Faint oscillatory-zoned plagioclase. D: Mafic lava

1356 groundmass, typically consisting of feldspar + olivine + magnetite ± clinopyroxene ±

1357 ilmenite; E: Unzoned feldspar typical of felsic products; F: Unzoned fayalitic olivine;

1358 G: Groundmass of felsic lavas flows consists dominantly of feldspar with minor

1359 interstitial aegirine and fayalite; H: Dark in BSE cristobalite with characteristic fish-

1360 scale textures replacing groundmass and some feldspar crystals.

1361 Figure 7: Ternary feldspar diagrams showing all feldspars differentiated by composition and

1362 eruptive style. For full data set see Electronic Appendix 2.

1363 Figure 8: Compositions of feldspars from (a) mafic to intermediate lavas; (b) felsic lavas and

1364 (c, d) all Ascension Island samples. Sample areas relate to those used in Table 1. For

1365 full data set see Electronic Appendix 2. The purple field on panel (b) shows the

compositions of feldspars from mafic to intermediate lava samples. The pink field on

panel (b) shows the Mid Atlantic Ridge ocean crust feldspars from the Kane Fracture

Zone (Coogan et al., 2000). Core-rim differences within individual samples shown by

filled (core) and open (rim) symbols in (c); sample colours and shapes refer to those

listed in the key on (c).

Figure 9: Variation in plagioclase (a) and olivine (b) compositions with whole rock SiO_2 (a)

or Mg# (b), and the calculated equilibrium compositions of the respective crystal

phases based on whole rock XRF data (Table 1, and Electronic Appendix 2). In (a)

equilibrium compositions of feldspar are calculated at 1150 °C and 330 MPa (black)

and 1050 °C and 330 MPa (grey) respectively, based on feldspar-melt and Fe-Ti oxide

thermometry (see Table 8), and the pressure at the base of the crust at Ascension Island

(Klingelhöfer, 2001).

Figure 10: Compositions of olivines from (a) mafic to intermediate lavas; (b) all pyroclastic

samples. Variations between core and rim compositions shown in panel (c), where open

symbols refer to rim analyses, and filled symbols core analyses. Sample areas relate to

those used in Table 1. For full data set see Electronic Appendix 2. The purple field on

(b) shows the compositions of olivines from mafic to intermediate lava samples.

Figure 11: Compositions of pyroxenes from all Ascension Island samples. Triangles refer to

samples of mafic to intermediate lava samples; squares and circles are felsic lava

samples. Sample areas relate to those used in Table 1. For full data set see Electronic

Appendix 2.

Figure 12: Matrix glass compositions from all Ascension Island samples. Sample areas relate

to those used in Table 1. For full data set see Electronic Appendix 2.

Figure 13: Combined liquid lines of descent modelled from AI14-438 (to 950 °C, end marked

by dashed line) and AI-621 (< 950 °C, start from dashed line) using rhyolite-MELTS

1391 (Gualda & Ghiorso, 2015) at 330 MPa, 250 MPa, 170 MPa and 90 MPa. Purple ticks

1392 mark 20% increments of melt fraction remaining; grey ticks mark 10% melt fraction

1393 remaining, black ticks show liquid composition at 5% melt fraction remaining. Initial

1394 water concentrations for AI-438 were 0.5 wt.% H_2O, from MAR glasses showing a

1395 component of the fertile mantle end member suggested to be the source of magmatism

1396 at Ascension Island (Almeev et al., 2008; Paulick et al., 2010). *XRF data used is a

1397 combination of data presented here and Weaver et al. (1996) and Kar (1997).

1398 Figure 14: Modelled fractionating crystal compositions from MELTS (purple symbols

1399 representing different pressures of crystallisation, Gualda & Ghiorso, 2015) compared

1400 with those measured in this study (grey symbols). The decompression trend (black

1401 crosses) represents isothermal decompression at 800 °C from 90 to 1 MPa.

1402 Figure 15: Trace element fractional crystallisation modelling following the stages modelling

1403 using Petrograph (Petrelli et al., 2005). XRF data used for the modelling shown in

1404 diamonds, the resultant modelled liquid as diamonds. Each stage (1 – 4, connected by

1405 dashed lines) represents 0.92, 0.40, 0.16, 0.07 total melt fraction remaining. *Total

1406 XRF data field in grey is a combination of data presented here, and Weaver et al., 1996

1407 and Kar, 1997. [1], [2]: For stages and full modelled compositions and references for

1408 partition coefficients used, see Electronic Appendix 3. The dashed field in (a)

1409 represents a subset of samples which plot towards syenitic samples of Ascension (not

1410 sampled in this study) and thus not modelled here.

1411 Figure 16: Magmatic plumbing system model for Ascension Island- magma storage regions

1412 are not to scale. Note the geographic variation in the distribution of plutonic bodies

1413 (mafic plutonics in blue, zone of nested felsic plutonics hashed, with examples in

1414 purple) within the crust. Ascent paths shown in red (mafic) and purple-blue (felsics).

1415 Crustal structure derived from Klingelhöfer et al. (2001).
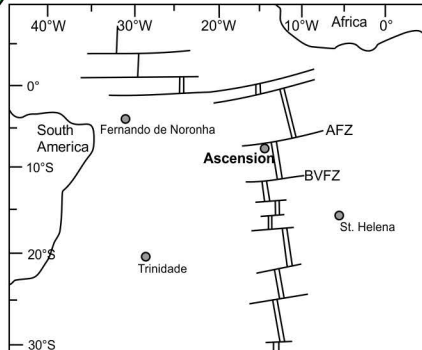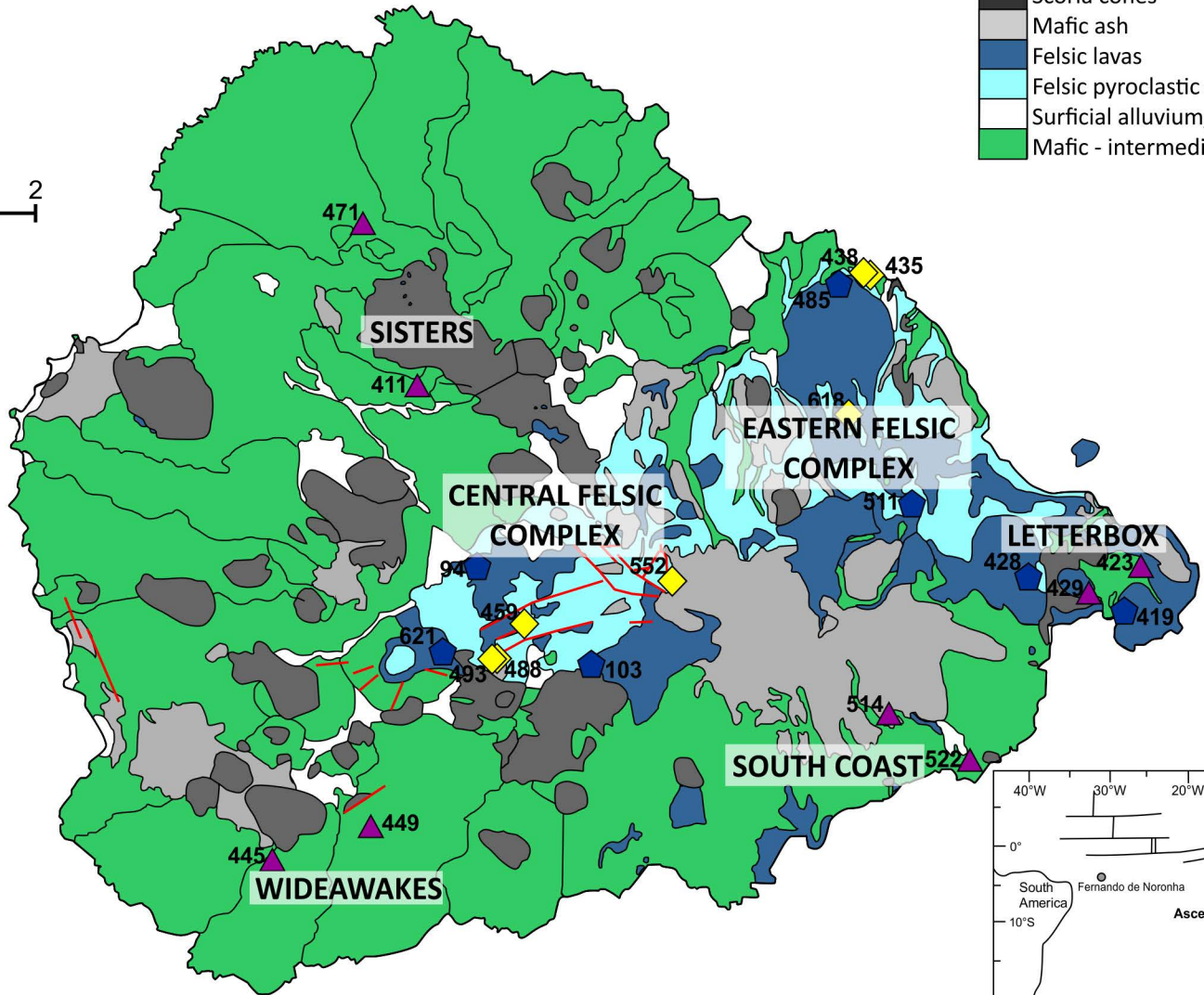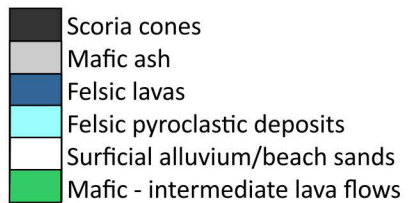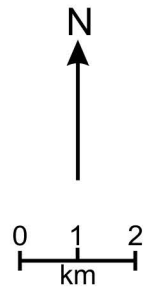
PPL
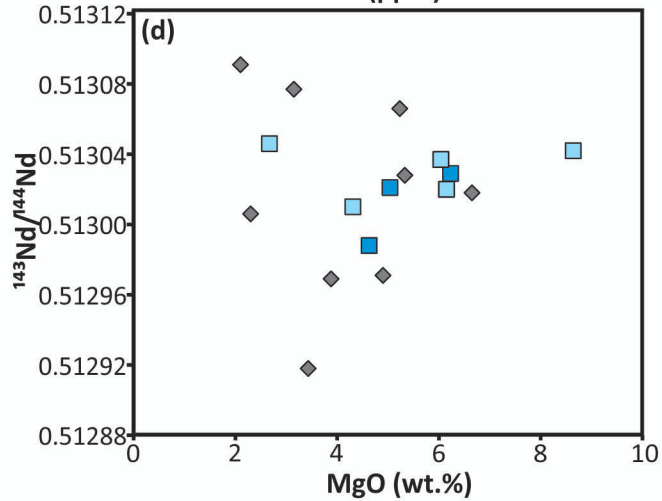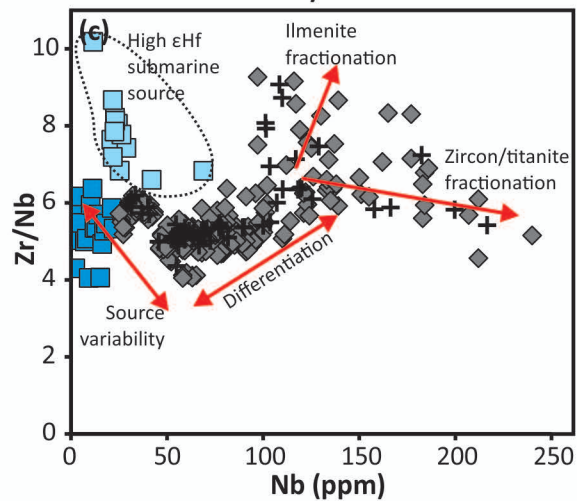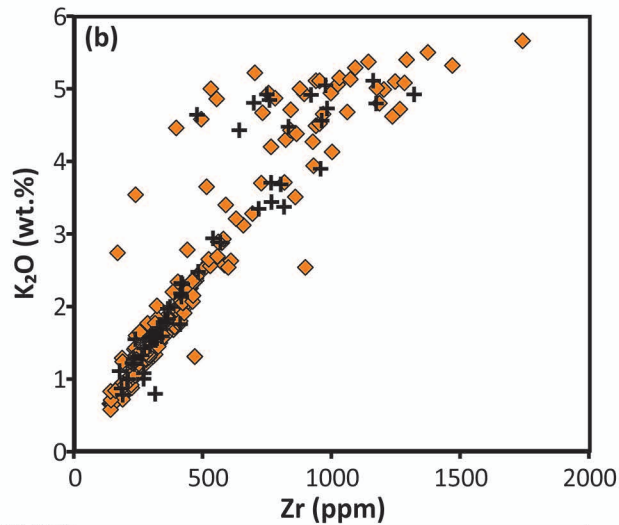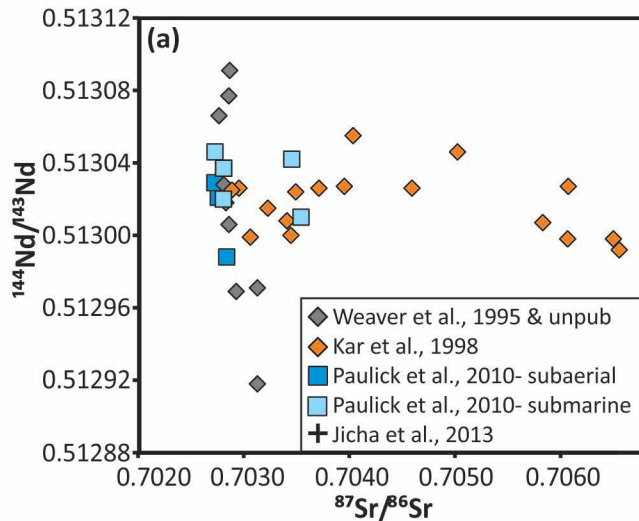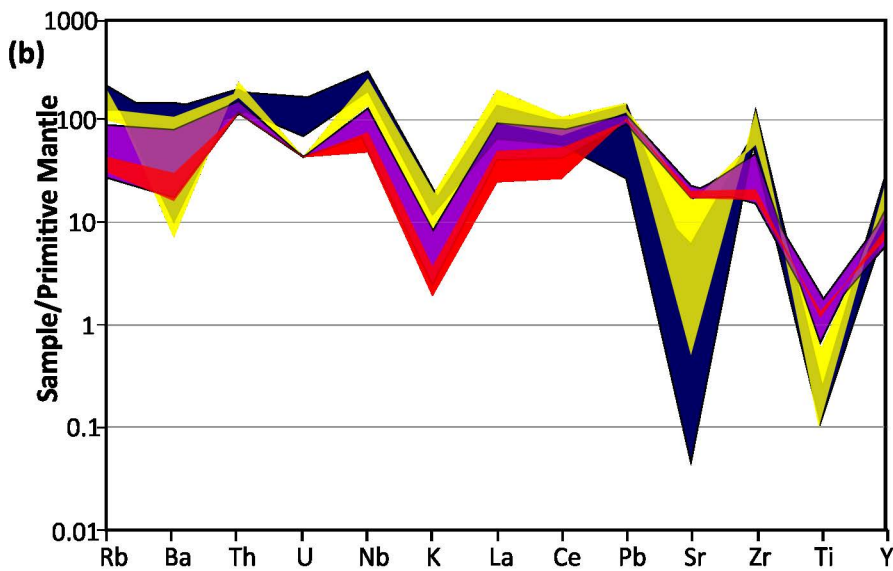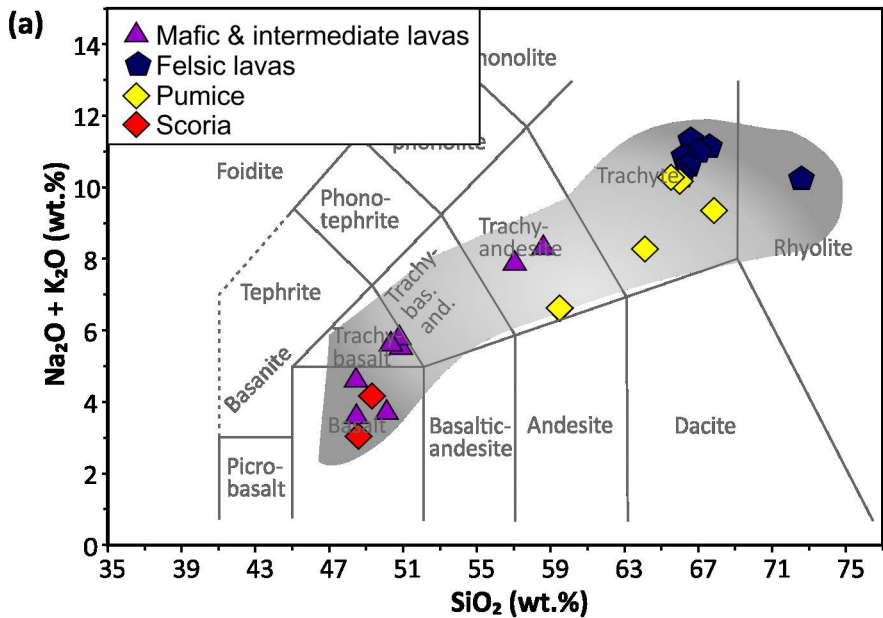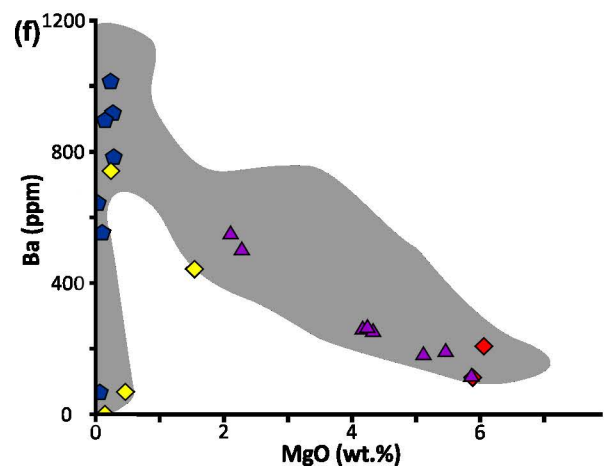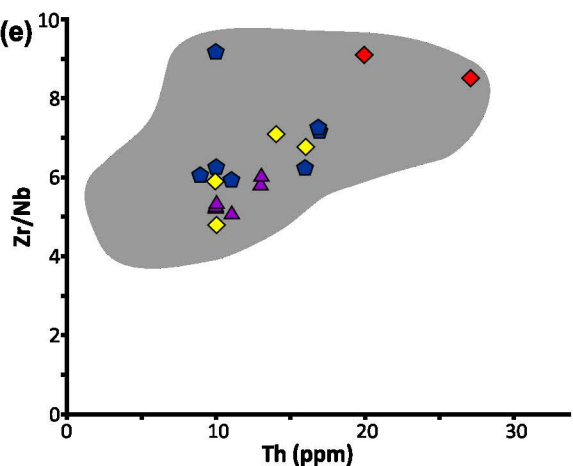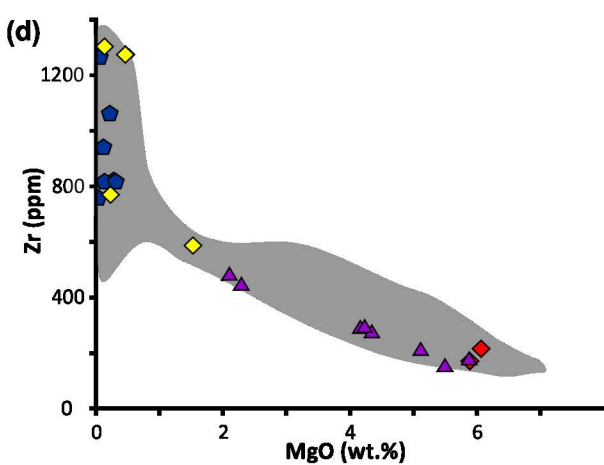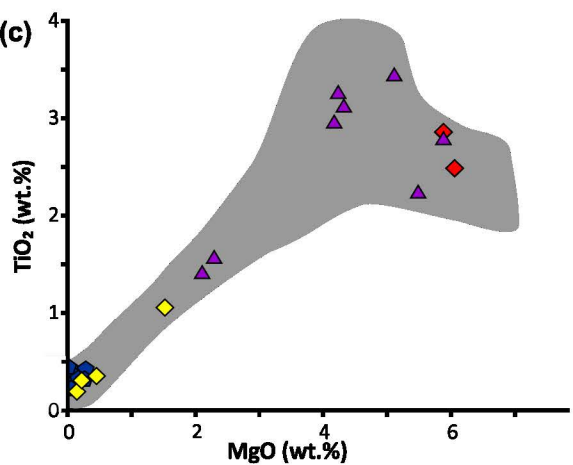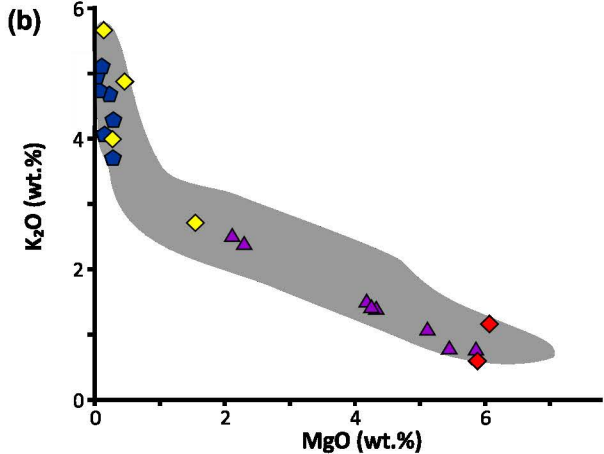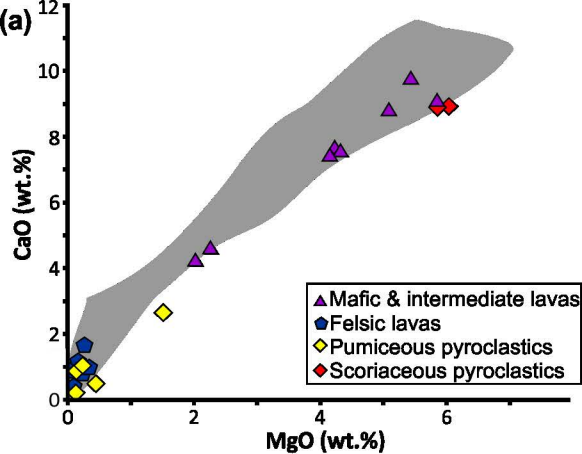
(a) AI14-522: South Coast [48.9 wt.%]
200 μm
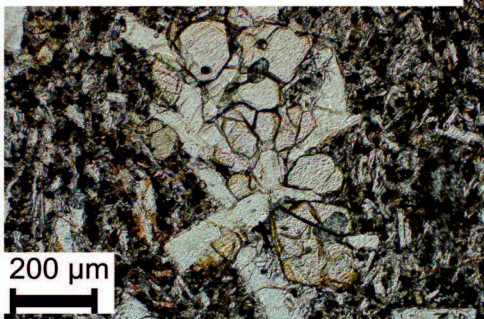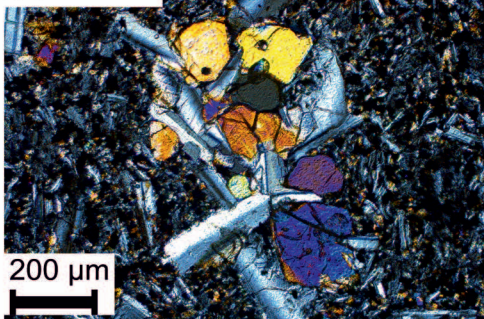
(c) AI14-411: Young Sisters [49.5 wt.%]
800 μm
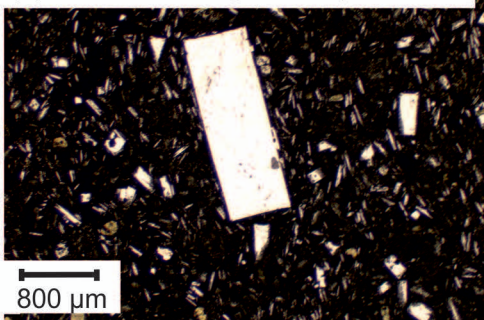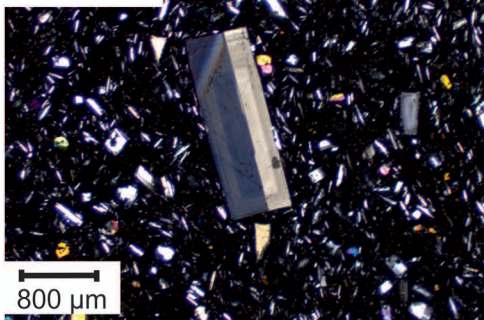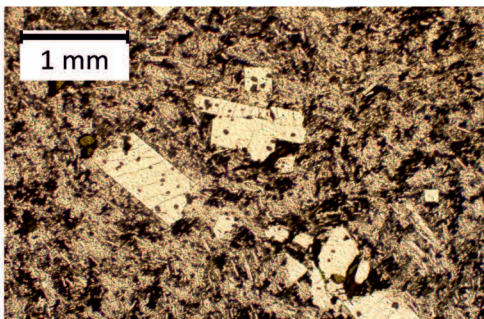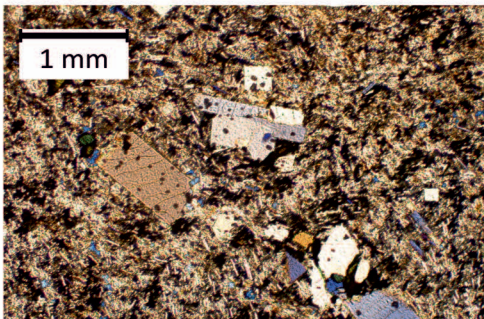
1 mm

(e) AI14-511: Cricket Valley [67.3 wt.%]

1 mm

(g) AI14-428: White Horse [66.8 wt.%]

XPL

(b) AI14-522
200 μm

(d) AI14-411
800 μm

1 mm

(f) AI14-511

1 mm

(h) AI14-485
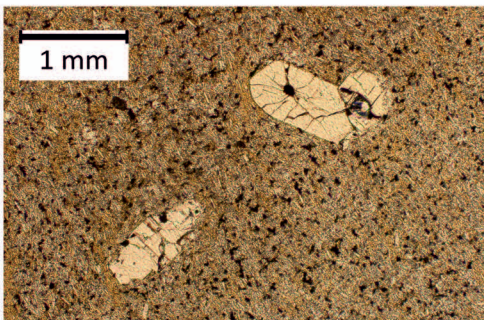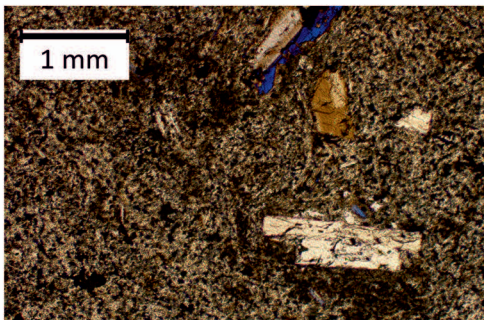
(a) AI-522: South Coast [48.9 wt.%]
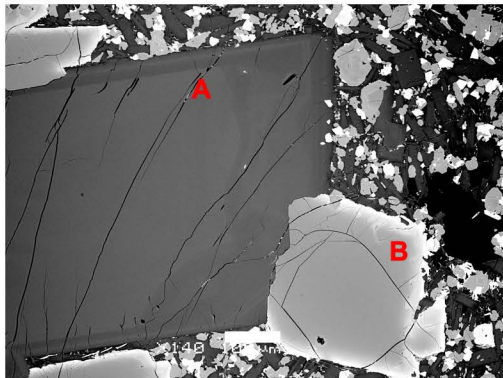
(b) AI-522: South Coast [48.9 wt.%]
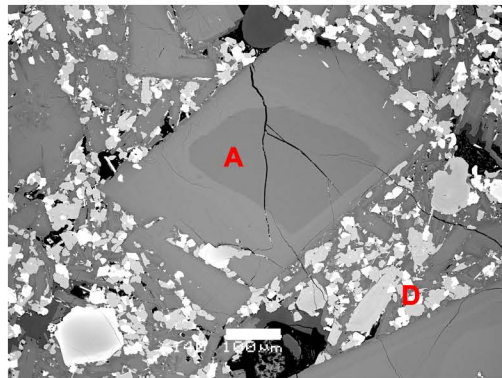
(c) AI-423: Letterbox [57.6 wt.%]

(d) AI14-428: White Horse [66.8 wt.%]

(e) AI-511: Cricket Valley [67.3 wt.%]

(f) AI-485: Ariane [65.9 wt.%]

An

Mafic lavas
Felsic lavas
Pumice
Scoria

Ab

Or

(a) Mafic lavas

Legend:
- Letterbox
- Wideawakes
- Sisters
- Older South Coast
- Younger South Coast

(b) Felsic lavas

Legend:
- Cricket Valley
- Ariane
- Letterbox felsic lava
- White Horse
- Mountain Red Hill
- Devils Riding School
- Middleton's Ridge

(c)

Legend:
- Letterbox
- Wideawakes
- Sisters
- South Coast
- Felsic lavas
- Pumice

(d)

(a) Mafic & Intermediate lavas

Legend:
- △ Letterbox
- ● Wideawakes
- ■ Sisters
- ◆ South Coast

X-axis: SiO_2 (wt.%)
Y-axis: Fo, %

(b) Pyroclastics

Legend:
- ● Youngest pumice fall
- ● Echo Canyon ignimbrite
- ◆ NE Bay scoria
- ● Compositionally-zoned[1]
- ◆ Green Mountain scoria
- △ NASA E fall
- △ NASA A fall
- ▲ Middletons Valley fall
- ■ Letterbox Comendite

X-axis: SiO_2 (wt.%)
Y-axis: Fo, %

(c) Core-rim variation

Legend:
- ◆ NE scoria- Cores
- ◇ NE scoria- Rims
- ● Echo Canyon- Cores
- ○ Echo Canyon- Rims
- △ NASA E- Cores
- △ NASA E- Rims
- ◆ South Coast (Y)-Cores
- ◇ South Coast (Y)- Rims
- ● Wideawakes (Y)- Cores
- ○ Wideawakes (Y)- Rims
- ▲ Letterbox (Y)- Cores
- △ Letterbox (Y) Rims

X-axis: Whole rock MgO (wt.%)
Y-axis: Fo, %

(a)

Legend:
- Youngest pumice fall
- Echo Canyon ignimbrite
- NE Bay scoria
- Compositionally-zoned[1]
- Green Mountain scoria
- NASA E fall
- NASA A fall
- Middletons Valley fall
- Letterbox felsic lava

CaO (wt.%) vs SiO$_2$ (wt.%)

(b)

Ba (ppm) vs SiO$_2$ (wt.%)

(c)

Th/U vs Rb/Sr

(a) Feldspar

Legend:
- ◆ 330 MPa model
- ■ 250 MPa model
- ● 170 MPa model
- ▲ 90 MPa model
- + Isothermal decompression
- ◆ Data (this study)

(b) Olivine

(c) Clinopyroxene

(a)

(b)

(c)

	XRF data field*
◆	XRF data stage 1-4[1]
▲	Modelled outputs stage 1-4[2]

WIDEAWAKES

SOUTH COAST

N

10 km

OVERTHICKENED MAFIC PLUTONICS

NORTHEASTERN
FELSIC COMPLEX

LAYER 2

Lower crustal zone of
nested discrete plutonic
bodies of variable composition

LAYER 3

12-13 km[1]

MOHO

ZONE OF MELT EXTRACTION

Table 1: Samples investigated for this study

Sample number	Region	TAS classification	Sample type	Grid Reference (E, N)	Approximate age of sample
AI14-411	Youngest Sisters	Trachy-basalt	mafic lava	0568706, 9123576	zero age *
AI14-471	Older Sisters	Trachy-basalt	mafic lava	0567966, 9125332	> AI14-411¥
AI14-423	Youngest Letterbox	Trachy-andesite	mafic lava	0577052, 9121328	- -
AI14-429	Older Letterbox	Trachy-andesite	mafic lava	0576443, 9121020	> AI14-423¥
AI14-445	Youngest Wideawakes	Basallt	mafic lava	0566907, 9117906	298 ka *
AI14-449	Older Wideawakes	Trachy-basalt	mafic lava	0568052, 9118271	> 298 ka ¥
AI14-522	Youngest South Coast	Basalt	mafic lava	0575056, 9119068	120 ka ""
AI14-514	Older South Coast	Basalt	mafic lava	0574092, 9119604	> 120 ka ¥
AI14-485	Ariane flow	Trachyte	felsic lava	0573518, 9124726	169 ka *
AI14-511	Cricket Valley	Trachyte	felsic dome	0574341, 0122098	52 ka *
AI14-428	White Horse	Trachyte	felsic dome	0575736, 9121232	zero age *
AI-94	Middleton's Ridge	Rhyolite	felsic lava	05693, 91214	1094 ka *
AI-103	Mountain Red Hill	Trachyte	felsic lava	05706, 91202	602 ka *
AI14-419	Letterbox felsic lava	Trachyte	felsic dome	0576780, 9120822	- -
AI15-621	Devil's Riding School	Trachyte	felsic dome	0568897, 9120365	652 ka*
AI15-618	Youngest pumice fall	Trachyte	pumice fall	0573646, 9123128	- -
AI14-435A	Echo Canyon	Trachyte	pumice flow	0573840, 9124754	- -
AI14-438	NE scoria	Basalt	scoria fall	0573786, 9124790	- -
AI14-493A	NASA unit E	Trachyte	pumice fall	0569420, 9120262	> AI14-488A ¥
AI14-488A	NASA unit A	Trachyte	pumice fall	0569475, 9120264	- -
AI14-459A	Middleton's Valley fall	Trachy-andesite	pumice fall	0569849, 9120661	- -
AI14-552	Green Mountain scoria	Basalt	scoria fall	0571584, 9121198	- -
AI14-439A+	*Compositionally-zoned top*	*Trachy-andesite*	*zoned fall*	*0573786, 9124790*	- -
AI14-439D+	*Compositionally-zoned mid*	*Trachy-andesite*	*zoned fall*	*0573786, 9124790*	
AI14-439G+	*Compositionally-zoned base*	*Trachyte*	*zoned fall*	*0573786, 9124790*	

[+] Data presented in Chamberlain et al., 2016.

* Ar-Ar age data from Jicha et al., 2014

"" K-Ar age data from Harris et al., 1992

¥ Stratigraphic relationship observed in the field

Table 2: Whole rock XRF data for Ascension samples, major elements in wt.%, trace elements in ppm.

Sample number	AI114-411	AI14-471	AI14-423	AI14-429	AI14-445	AI14-449	AI14-522	AI14-514	AI14-485	AI14-511	AI14-428	AI-94	AI-103
Location	Young Sisters	Old Sisters	Young Letterbox	Old Letterbox	Younger Wideawakes	Older Wideawakes	Younger South Coast	Older South Coast	Ariane	Cricket Valley	White Horse	Middleton's Mountain Ridge	Red Hill
SiO_2	49.5	49.6	57.6	55.8	47.3	49.2	48.9	47.0	65.9	67.3	66.8	72.5	66.6
TiO_2	3.12	2.97	1.42	1.58	3.44	3.26	2.25	2.79	0.42	0.37	0.41	0.23	0.45
Al_2O_3	15.5	15.5	16.9	16.7	15.3	15.2	16.1	15.5	16.1	15.3	15.5	12.7	15.5
Fe_2O_3	12.5	12.2	8.23	8.63	13.8	12.8	10.8	13.0	4.97	4.62	4.68	3.70	5.85
MnO	0.22	0.22	0.24	0.23	0.20	0.23	0.16	0.18	0.22	0.16	0.18	0.12	0.12
MgO	4.33	4.16	2.10	2.29	5.11	4.24	5.46	5.87	0.28	0.11	0.28	0.06	0.04
CaO	7.55	7.42	4.23	4.62	8.80	7.70	9.8	9.13	1.6	0.88	1.04	0.33	0.38
Na_2O	4.03	4.18	5.68	5.40	3.45	4.09	2.85	2.76	6.62	6.07	6.73	5.60	6.04
K_2O	1.41	1.50	2.53	2.37	1.08	1.44	0.80	0.77	3.71	5.11	4.30	4.72	4.94
P_2O_5	0.89	1.03	0.60	1.04	0.81	1.18	0.53	0.4	0.09	0.06	0.09	0.03	0.06
LOI	-0.10	-0.02	-0.45	-0.51	-0.21	-0.34	0.24	-0.14	0.12	0.00	0.15	0.37	0.95
Total	99.0	98.8	99.0	98.1	99.1	98.9	97.8	97.3	100.1	100.0	100.2	100.4	101.0
Ba	254	263	553	503	183	266	194	120	780	554	919	69	644
Rb	32	34	53	50	24	29	17	16	76	117	94	126	81
Sr	455	461	381	410	423	458	501	391	135	7	24	1	4
Pb	18	20	20	21	17	19	bdl	bdl	5	8	6	10	5
Th	10	10	13	13	11	10	bdl	bdl	9	16	11	17	10
U	bdl	bdl	1	1	1	1	bdl	bdl	bdl	3.7	1.6	bdl	2.0
Zr	279	291	483	450	214	292	158	182	818	940	823	1266	756
Nb	52	55	80	77	42	54	28	29	135	151	139	177	121
Y	41	44	54	52	27	49	24	30	85	62	45	113	57
La	34	35	64	56	28	41	bdl	bdl	71	53	50	78	45
Ce	96	105	144	140	74	115	61	49	156	119	112	177	100
Sc	21	19	12	12	24	18	26	28	9	9	8	3	12
V	227	203	42	55	317	208	252	314	3	4	7	4	3
Ni	8	5	3	5	24	3	56	65	5	3	4	6	5
Zn	122	128	128	132	115	130	83	105	150	126	136	197	151

Sample number	AI114-419	AI15-621	AI15-618	AI14-435A	AI14-438	AI14-493A	AI14-488A	AI14-459A	AI14-552
Location	Letterbox Felsic lava	Devils Riding School	Youngest Pumice fall	Echo Canyon	NE scoria	NASA unit E	NASA unit A	Middleton's Valley fall	Green Mountain scoria
SiO_2	65.5	66.9	65.0	65.6	48.2	68.1	64.3	58.5	47.7
TiO_2	0.32	0.33	0.33	0.31	2.49	0.18	0.33	1.06	2.85
Al_2O_3	15.9	15.4	13.7	15.7	16.1	13.1	14.5	17.6	16.0
Fe_2O_3	4.58	4.41	4.05	4.34	11.5	3.74	5.18	5.59	13.4
MnO	0.17	0.17	0.16	0.20	0.19	0.11	0.19	0.16	0.18

MgO	0.15	0.22	0.16	0.23	6.06	0.14	0.46	1.53	5.88
CaO	0.87	1.03	0.80	1.08	8.93	0.21	0.49	2.65	8.90
Na_2O	6.48	6.76	5.23	6.35	2.95	3.78	3.47	3.84	2.41
K_2O	4.06	4.68	4.84	4.00	1.15	5.66	4.88	2.72	0.60
P_2O_5	0.57	0.04	0.07	0.04	0.94	0.02	0.03	0.37	0.31
LOI	0.27	0.93	4.57	2.70	-0.56	5.73	6.90	4.68	0.15
Total	98.9	100.9	98.9	100.5	97.9	100.8	100.7	98.7	98.3
Ba	898	1011	49	740	207	bdl	68	446	111
Rb	75	88	121	77	26	139	105	61	19
Sr	83	15	50	79	446	bdl	11	338	381
Pb	26	5	bdl	24	18	27	24	22	19
Th	17	10	20	16	10	27	20	14	10
U	2	3.4	bdl	bdl	1	bdl	bdl	1	1
Zr	818	1062	948	770	216	1301	1276	589	171
Nb	114	116	147	114	45	152	140	83	29
Y	76	73	89	72	35	96	88	52	28
La	95	57	109	91	34	135	127	64	17
Ce	157	117	173	162	94	188	186	124	47
Sc	6	10	bdl	bdl	23	bdl	bdl	6	28
V	2	4	bdl	bdl	209	bdl	bdl	34	307
Ni	3	7	bdl	bdl	65	bdl	bdl	6	45
Zn	138	145	141	142	111	171	179	103	105

Table 3: Petrography of Ascension lavas

Sample number	Region	TAS classification	Percentage Phenocrysts*	Vesicularity (%)	Fspar	Ol	Cpx	Cbt	Aeg	Glass	Ox+Accessory
AI14-411	Youngest Sisters	Trachy-basalt	<1 (f)	5	67	5	20				8
AI14-471	Older Sisters	Trachy-basalt	<1 (f)	7	68	10	17				5
AI14-445	Youngest Wideawakes	Basallt	3 (f, ol)	3	68	14	12				6
AI14-449	Older Wideawakes	Trachy-basalt	<1 (f, ol)	6	55	9	32				4
AI14-423	Youngest Letterbox	Trachy-andesite	<1 (f)	5	80	6	10				4
AI14-429	Older Letterbox	Trachy-andesite	2 (f)	43	77	8	9				6
AI14-522	Youngest South Coast	Basalt	40 (f, ol)	3	62	31	<1				7
AI14-514	Older South Coast	Basalt	18 (f, ol)	23	56	23					21
AI14-428	White Horse	Trachyte	2 (f)	24	64			29	4		3
AI14-511	Cricket Valley	Trachyte	6 (f, aeg)	1	78			12	9		1
AI14-485	Ariane flow	Trachyte	4 (f)	15	77			19			4
AI14-419	Letterbox felsic lava	Trachyte	<1 (f)	25	60		1	1		37	1
AI-103	Mountain Red Hill	Trachyte	2 (f, ox)	4	70			24	5		1
AI15-621	Devil's Riding School	Trachyte	3 (f)	13	68			27	4		1
AI-94	Middleton's Ridge	Rhyolite	<1 (f)	18	57			35	6		2

Arranged by relative age (see Table 1 and references therein)

Crystal percentages represent groundmass (<500 μm) crystals as well as those represented as phenocryst phases; Fspar = feldspar (plagioclase and ternary); Ol = olivine; Cpx = clinopyroxene; Cbt = cristobalite; Aeg = aegirine; Ox+Acc = bright in Back Scattered Electron imagery oxides and accessory phases including zircon and apatite.

*Phenocrysts used to represent phases > 500 μm in thin sectioned area. Phases which constitute phenocryst phases indicated in brackets: f= feldspar, ol = olivine; cpx = clinopyroxene; aeg = aegirine; ox = oxides;

Table 4: Representative feldspar data for Ascension samples

Sample	AI114-411				AI14-423		AI14-445		AI14-522		AI14-485		
Location	Young Sisters				Young Letterbox		Young Wideawakes		Young South Coast		Ariane		
Rock type	Trachy-basalt				Trachy-andesite		Basalt		Basalt		Trachyte		
Spot location	F3-C	F3-R	F5-C	F5-R	F1-C	F1-R	F5-C	F5-R	F1-C	F1-R	K3-C	K3-R	K10-C
SiO_2	53.50	53.29	47.46	52.69	56.56	56.19	52.57	51.22	48.05	51.89	63.33	61.71	62.46
TiO_2	0.16	0.17	0.05	0.13	0.04	0.06	0.13	0.16	0.05	0.10	0.00	0.01	0.01
Al_2O_3	28.26	28.18	32.79	29.25	26.89	26.57	28.59	29.16	32.44	29.44	22.67	23.21	23.19
FeO*	0.91	0.92	0.45	0.77	0.37	0.49	0.77	0.87	0.46	0.66	0.20	0.24	0.25
MgO	0.10	0.09	0.13	0.11	0.04	0.05	0.12	0.13	0.15	0.15	0.00	0.01	0.01
CaO	11.45	11.61	16.66	12.19	8.93	8.88	12.20	12.80	15.92	13.46	3.48	4.44	4.28
Na_2O	5.04	5.10	2.30	4.74	6.55	6.63	4.48	4.29	2.67	4.17	9.17	8.56	8.87
K_2O	0.32	0.33	0.07	0.26	0.36	0.36	0.24	0.23	0.10	0.18	1.26	1.17	0.83
Total	99.76	99.70	99.91	100.15	99.75	99.23	99.10	98.87	99.86	100.05	100.11	99.34	99.90
An	54.6	54.7	79.7	57.8	42.1	41.7	59.3	61.4	76.3	63.4	16.1	20.8	20.0
Ab	43.5	43.5	19.9	40.7	55.9	56.3	39.3	37.2	23.1	35.6	76.9	72.7	75.3
Or	1.8	1.9	0.4	1.5	2.0	2.0	1.4	1.4	0.6	1.0	7.0	6.5	4.7
Sc	4.55	4.90	4.64	4.60	4.6	3.11	6.38	12.0	8.48	7.22	6.60	5.20	8.00
Ti	421	612	696	664	254	344	797	4970	508	526	136	137	147
V	0.53	1.60	1.73	1.58	0.42	0.51	3.49	83	3.12	2.41	0.16	bdl	0.48
Mn	32.8	32.6	36.5	38.8	37.7	36.9	37.9	323	37.8	28.3	27.0	25.0	27.0
Ga	21.2	20.0	24.9	23.0	24.8	26.0	24.7	22.9	23.1	23.1	28.2	27.1	26.8
Rb	0.31	0.45	0.28	0.14	0.86	0.56	0.93	2.90	0.24	0.32	1.56	1.64	1.29
Sr	1130	1096	1104	1168	1289	1317	922	811	793	718	834	883	836
Y	0.19	0.18	0.20	0.40	0.64	0.40	0.57	9.00	0.11	0.08	0.02	0.13	0.13
Zr	0.41	0.22	0.00	0.11	2.80	1.54	1.26	31.5	0.50	0.17	bdl	1.86	0.25
Ba	134	137	121	175	295	324	109	131	70.7	86.2	1248	1353	1087
La	3.16	2.76	2.46	2.71	5.88	6.40	2.13	9.23	1.08	1.10	8.29	7.78	7.35
Ce	5.21	3.73	3.61	4.33	8.62	6.47	4.00	20.0	1.93	1.55	9.14	9.42	8.43
Pr	0.54	0.41	0.24	0.42	0.90	0.81	0.37	2.33	0.17	0.18	0.74	0.57	0.60
Nd	2.24	0.99	1.00	1.55	2.10	2.36	1.72	11.4	0.59	0.70	1.71	1.80	1.51
Sm	0.23	0.09	0.34	0.41	0.57	0.19	0.31	2.37	0.04	bdl	0.13	0.00	0.17
Eu	1.07	0.68	0.78	0.98	3.04	2.50	0.68	1.21	0.38	0.39	8.97	9.59	9.15
Gd	0.17	0.27	0	0.25	0.35	0.20	0.25	2.44	bdl	0.06	bdl	0.21	0.17
Yb	bdl	bdl	bdl	bdl	0.13	bdl	0.01	0.61	0.02	bdl	0.00	0.00	0.00
Pb	0.40	0.22	0.26	0.22	0.84	0.65	0.23	0.63	0.22	0.10	1.04	1.01	0.84

Sample	AI114-485	AI14-511		AI14-419		AI14-435A		AI14-493A		AI14-488A		AI14-459A		
Location	Ariane	Cricket Valley		Letterbox felsic lava		Echo Canyon		NASA Unit E		NASA Unit A		Middletons Valley		
Rock type	Trachyte	Trachyte		Trachyte		Trachyte		Trachyte		Trachyte		Trachy-andesite		
Spot location	F10-R	F2-C	F2-R	F3-C	F3-R	F4-C	F4-R	F26-C	F26-R	K13-C	K13-R	K18-C	K18-R	K20-C
SiO_2	65.60	65.20	65.89	65.20	64.76	65.21	65.91	67.98	68.53	68.51	67.88	62.04	61.39	58.09
TiO_2	0.03	0.02	0.01	0.00	0.00	0.00	0.01	0.00	0.00	0.00	0.01	0.02	0.07	0.04
Al_2O_3	19.42	19.33	19.00	20.71	20.90	21.22	20.57	19.24	19.53	19.36	19.31	22.50	23.09	24.64
FeO*	0.53	0.32	0.31	0.17	0.20	0.22	0.18	0.29	0.24	0.28	0.32	0.34	0.49	0.35
MgO	0.00	0.00	0.00	0.00	0.00	0.00	0.00	0.00	0.00	0.01	0.00	0.03	0.03	0.04
CaO	0.75	0.23	0.07	1.44	1.67	3.21	2.59	0.07	0.12	0.13	0.12	5.10	5.86	7.59
Na_2O	8.56	7.79	7.74	9.19	9.13	8.96	9.28	7.50	7.73	7.53	8.03	8.28	7.96	7.29
K_2O	4.37	6.30	6.54	2.40	2.46	1.12	1.40	6.64	6.36	6.08	5.92	0.94	0.74	0.48
Total	99.28	99.22	99.57	99.10	99.14	99.95	99.93	101.71	102.52	101.89	101.58	99.25	99.62	98.52
An	3.5	1.1	0.3	6.9	7.9	15.5	12.3	0.3	0.6	0.6	0.6	24.1	27.7	35.5
Ab	72.2	64.6	64.1	79.4	78.2	78.1	79.8	63.0	64.5	64.9	67.0	70.6	68.1	61.8
Or	24.3	34.4	35.6	13.7	13.9	6.4	7.9	36.7	34.9	34.5	32.4	5.3	4.2	2.7
Sc	6.90	6.77	7.44	0.33	6.97	3.90	5.20	6.30	3.20	5.20	6.90	5.20	4.20	3.60
Ti	156	104	76.5	6.89	124	105	104	62.0	84.0	69.8	67.7	229	264	352
V	0.31	0.45	0.17	0.02	bdl	0.11	bdl	bdl	1.70	0.09	0.01	bdl	1.40	1.70
Mn	20.1	1.20	0.60	2.55	7.00	22.1	11.8	1.10	bdl	2.10	bdl	19.9	28.0	34.8
Ga	27.8	25.6	24.5	0.95	28.7	28.0	25.9	32.2	34.7	30.7	35.3	29.5	23.5	33.9
Rb	2.40	39.0	47.3	0.33	10.2	2.06	1.91	51.2	45.7	32.8	33.0	1.56	2.16	1.18
Sr	828	1.31	0.81	13.0	222	644	571	0.79	2.28	2.35	1.46	1169	1230	1930
Y	0.31	0.17	0.03	0.19	0.79	0.04	0.00	0.00	0.00	0.00	0.00	0.10	0.27	0.36
Zr	2.70	3.22	0.45	2.17	bdl	0.00	0.00	bdl	2.90	0.30	0.47	bdl	5.50	1.80
Ba	1261	120	80.6	96.7	3770	1680	1552	66.0	129	194	97.4	533	753	448
La	8.60	0.67	0.42	0.48	6.96	7.35	6.03	0.65	0.66	0.43	0.56	11.6	12.4	11.7
Ce	9.90	0.68	0.23	0.73	8.47	8.37	7.14	0.13	0.30	0.37	0.17	15.2	14.2	15.9
Pr	0.74	0.02	bdl	0.07	0.72	0.48	0.52	0.00	0.00	0.00	0.00	1.01	1.14	0.85
Nd	2.40	0.27	0.04	0.28	2.20	1.47	1.24	0.00	0.00	0.00	0.00	3.10	3.60	3.10
Sm	0.26	0.03	bdl	0.05	0.22	0.00	0.00	0.00	0.00	0.00	0.00	0.00	0.00	0.27
Eu	9.82	0.98	0.99	0.28	7.07	8.85	8.50	0.73	1.00	1.25	1.00	2.27	3.65	3.53
Gd	0.18	0.01	bdl	0.04	0.35	0.00	0.00	0.00	0.00	0.00	0.00	0.00	0.04	0.00
Yb	0.00	bdl	bdl	0.02	0.00	0.00	0.00	0.00	0.00	0.00	0.00	0.00	0.00	0.00
Pb	1.21	1.12	0.93	0.07	1.94	1.29	1.34	0.53	0.88	0.89	0.69	1.91	1.85	1.02

Major element data given as wt.%; Anorthite, albite and orthoclase (An, Ab, Or) contents as mol. %; trace elements in ppm. For full data set, see Electronic Appendix 2. Where elements are below the detection limits of the method, bdl is written. Spot location refers to the analysis being core [C] or rim [R].

Table 5: Representative olivine major and trace element data for selected Ascension samples

Sample	AI14-411		AI14-423		AI14-445		AI14-522		AI14-435A		AI14-493A	
Location	Young Sisters		Young Letterbox		Young Wideawakes		Young South Coast		Echo Canyon		NASA unit E	
Rock type	Trachy-basalt		Trachy-andesite		Basalt		Basalt		Trachyte		Trachyte	
Spot tag	16_C	16_R	2_C	2_R	6_C	6_R	6_C	6_R	3_C	3_R	10_C	10_R
SiO_2	39.59	38.43	35.49	35.07	38.96	37.31	37.93	37.17	29.42	29.23	28.74	29.11
Al_2O_3	0.06	0.00	0.02	0.02	0.03	0.03	0.03	0.04	0.00	0.00	0.00	0.00
FeO*	14.67	24.67	32.21	32.30	19.05	28.37	22.89	29.63	59.56	59.01	62.61	61.38
MnO	0.22	0.76	1.10	1.13	0.25	0.48	0.33	0.56	4.96	4.94	5.53	5.48
MgO	43.65	34.97	30.98	30.87	41.46	34.30	38.63	32.92	3.77	3.73	0.83	0.98
CaO	0.22	0.26	0.18	0.18	0.25	0.26	0.34	0.32	0.31	0.32	0.31	0.52
Cr_2O_3	0.03	bdl	0.00	0.00	0.01	0.00	0.00	0.00	0.00	0.00	0.00	0.00
NiO	0.19	0.00	0.01	0.00	0.15	0.04	0.07	0.05	0.02	0.00	0.00	0.00
P_2O_5	--	--	0.10	0.04	0.01	0.04	0.01	0.03	--	--	--	--
Total	98.63	99.16	100.15	99.65	100.19	100.83	100.25	100.73	98.04	97.24	98.02	97.48
Fo (%)	84.1	71.7	63.2	63.0	79.5	68.3	75.1	66.5	10.1	10.1	2.3	2.8
Fa (%)	15.9	28.3	36.8	37.0	20.5	31.7	24.9	33.5	89.9	89.9	97.7	97.2

Major element data given as wt.%; Fosterite, fayalite contents as mol. %. For full data set, see Electronic Appendix 2. Spot location refers to the analysis being core [C] or rim [R].

Table 6: Representative clinopyroxene major element data for selected Ascension samples

Sample	AI14-423		AI14-429		AI14-449		AI14-522		AI14-485	AI14-511		AI14-428		AI14-419		AI15-621		AI15-618	
Location	Young Letterbox		Old Letterbox		Old Wideawakes		Young South Coast		Ariane	Weatherpost		White Horse		Letterbox bedrock		Devils Riding School		Young pumice fall	
Rock type	Trachy-andesite		Trachy-andesite		Trachy-basalt		Basalt		Trachyte	Trachyte		Trachyte		Trachyte		Trachyte		Trachyte	
Spot tag	2_C	2_R	GM	GM	1_C	1_R	1_C	1_R	GM	GM	GM	GM	GM	1_C	1_R	GM	GM	10_C	10_R
SiO_2	48.35	50.51	49.37	36.12	50.22	48.46	50.63	47.34	47.79	47.74	47.90	50.81	50.86	48.50	48.20	47.94	49.82	51.82	51.58
TiO_2	1.27	0.75	0.97	0.02	0.96	2.25	1.09	1.94	2.05	0.29	0.42	1.95	1.88	0.39	0.53	0.32	0.47	0.63	0.56
Al_2O_3	3.62	1.98	3.03	0.02	2.15	5.37	2.82	5.19	2.59	0.29	0.33	2.35	3.50	0.70	0.89	0.21	1.99	1.59	1.69
FeO*	9.50	9.65	12.42	31.46	11.76	9.61	8.44	8.11	25.67	26.08	26.72	27.00	24.79	22.35	22.84	27.99	26.35	11.30	10.81
MnO	0.47	0.61	0.72	1.09	0.67	0.25	0.19	0.15	2.38	1.54	1.64	1.25	1.25	1.52	1.47	1.37	0.91	0.72	0.67
MgO	13.93	14.33	12.66	30.88	15.56	13.23	16.29	13.92	3.21	2.71	2.97	0.84	1.12	5.04	5.26	1.17	0.86	15.26	13.92
CaO	20.54	20.55	19.84	0.14	17.24	20.05	19.86	21.74	13.17	19.05	18.26	2.19	2.41	20.41	20.30	15.64	10.73	18.70	20.34
Na_2O	0.49	0.50	0.55	0.01	0.46	0.56	0.29	0.39	2.09	1.04	1.01	11.76	11.88	0.51	0.53	4.78	6.50	0.43	0.50
K_2O	0.00	0.03	0.00	0.00	0.01	0.00	0.00	0.01	0.09	0.00	0.00	0.70	1.24	0.01	0.01	1.39	2.06	0.00	0.01
Cr_2O_3	0.00	0.00	0.00	0.00	0.00	0.00	0.13	0.23	0.00	0.00	0.00	bdl	bdl	0.00	bdl	bdl	0.00	0.00	0.00
Total	98.16	98.91	99.58	99.74	99.03	99.78	99.76	99.02	99.05	98.74	99.25	98.85	98.94	99.44	100.02	100.81	99.69	100.45	100.09

Major element data given as wt.%. For full data set, see Electronic Appendix 2. Spot location refers to the analysis being core [C], rim [R] or groundmass [GM].

Table 7: Representative glass analyses from Ascension Island

7a: Major element analyses normalised to 100 wt.%

Sample	AI14-419		AI15-618		AI14-552		AI14-438		AI14-435A			AI14-493A		AI14-488A		AI14-459A	
Location	Letterbox felsic lava		Young pumice		Green Mountain sc.		NE scoria		Echo Canyon			NASA unit E		NASA unit A		Middelton's Valley fall	
Spot Tag	419-1	419-2	15-5	15-6	1-1	1-4	14-1	14-2	10-2	10-3	10-4	8-1	8-4	15-1	15-2	4-1	4-3
SiO$_2$	71.21	72.69	70.64	70.74	48.91	49.14	50.79	50.99	67.86	69.22	67.98	71.17	71.30	71.07	70.11	67.23	67.60
TiO$_2$	0.27	0.31	0.19	0.19	3.68	3.72	3.61	3.52	0.10	0.29	0.22	0.21	0.22	0.17	0.18	0.48	0.49
Al$_2$O$_3$	12.04	10.48	13.26	12.91	13.51	13.87	13.54	12.90	17.98	13.88	16.01	12.33	11.78	13.67	13.60	16.80	16.64
FeO*	5.64	5.77	4.50	4.89	13.53	13.27	12.02	11.97	1.38	4.47	3.43	4.77	4.87	3.28	3.96	2.78	2.94
MnO	0.27	0.28	0.27	0.25	0.15	0.23	0.19	0.20	0.08	0.19	0.16	0.18	0.16	0.12	0.20	0.07	0.06
MgO	0.06	0.07	0.03	0.02	5.32	5.41	3.78	4.52	0.02	0.08	0.09	0.02	0.02	0.00	0.00	0.54	0.50
CaO	0.77	0.51	0.48	0.46	9.70	9.43	7.91	8.56	0.65	0.64	0.90	0.29	0.28	0.46	0.45	1.32	1.23
Na$_2$O	5.15	4.44	6.14	6.11	3.34	3.16	3.48	3.22	7.32	5.43	6.09	5.52	4.42	4.42	4.95	5.88	5.73
K$_2$O	4.56	5.41	4.46	4.40	1.20	1.10	2.19	2.21	4.36	5.03	4.47	4.75	5.94	6.14	5.74	4.41	4.43
BaO	0.00	0.00	0.00	0.00	0.05	0.07	0.08	0.06	0.11	0.06	0.09	0.04	0.00	0.00	0.00	0.09	0.04
P$_2$O$_5$	0.03	0.04	0.03	0.01	0.57	0.56	1.97	1.74	0.04	0.01	0.00	0.03	0.01	0.04	0.01	0.11	0.10
Cl	0.00	0.00	0.00	0.00	0.04	0.05	0.11	0.12	0.11	0.43	0.34	0.54	0.60	0.56	0.54	0.25	0.24
F	0.00	0.00	0.00	0.00	0.00	0.00	0.33	0.00	0.00	0.27	0.22	0.14	0.40	0.07	0.26	0.03	0.00
Total	100	100	100	100	100	100	100	100	100	100	100	100	100	100	100	100	100

Major element data given as wt.%. For full data set, see Electronic Appendix 2.

Table 7b: Selected trace element data from glass in felsic samples (all elements in ppm); where elements are below the detection limits of the method, bdl is written. Analyses in italics previously published in Chamberlain et al., 2016.

Sample	AI14-419		AI14-435A		AI14-493A		AI14-459A			*AI14-439D*		*AI14-439G*		
Location	Letterbox felsic lava		Echo Canyon		NASA unit E		Middelton's Valley fall			*Compositionally-zoned mid (D) and upper (G)*				
Tag	G1	G2	G1	G2	G1	G2	G1	G2	G3	G1	G2	G1	G2	G3
Li	10.0	15.0	10.0	17.0	15.5	29.0	24.0	bdl	13.0	*13.6*	*18.0*	*29.0*	*20.0*	*18.0*
Sc	13.6	15.9	13.8	12.8	9.70	9.40	5.00	11.1	13.0	*11.2*	*21.0*	*27.0*	*10.1*	*27.0*
Ti	994	1020	1705	1300	1448	1437	5400	4960	5400	*2360*	*5690*	*4200*	*4530*	*2900*
V	1.60	1.20	0.71	bdl	4.37	6.80	10.1	10.0	21.0	*bdl*	*5.30*	*1.10*	*33.8*	*11.0*
Mn	863	820	1544	1290	1259	1270	1720	1060	1190	*1160*	*2720*	*2130*	*1290*	*1550*
Zn	84	90	154	215	268	239	178	113	94	*97*	*164*	*134*	*107*	*155*
Ga	34	32	30	32	39	42	57	38	33	*16*	*37*	*35*	*27*	*17*
Rb	101	58	90	90	169	182	166	134	161	*44*	*73*	*97*	*56*	*64*
Sr	90	106	50	44	10	8	246	175	220	*175*	*390*	*184*	*117*	*159*
Y	76	49	77	80	124	129	52	44	38	*34*	*74*	*70*	*41*	*79*
Zr	930	584	791	868	1507	1661	1180	1000	1310	*286*	*620*	*760*	*490*	*830*
Nb	133	89	147	161	234	247	160	135	141	*64*	*138*	*141*	*83*	*98*
Ba	746	1240	790	720	55	61	950	651	1020	*470*	*900*	*1290*	*840*	*1300*
La	76	51	83	83	138	145	93	65	71	*41*	*73*	*81*	*54*	*79*
Ce	160	113	169	178	274	283	197	124	145	*75*	*160*	*153*	*102*	*153*
Pr	18	12	19	20	30	30	17	12	9	*7*	*19*	*15*	*12*	*19*

Nd	67	50	73	77	112	115	57	43	45	*33*	*85*	*60*	*43*	*75*
Sm	16.9	9.3	15.3	14.8	24.2	23.9	13.6	8.2	7.8	*8*	*12.9*	*14.8*	*8.5*	*10.2*
Eu	2.67	3.92	3.24	2.52	2.61	2.40	2.57	2.40	2.60	*1.72*	*4.60*	*4.40*	*3.06*	*3.60*
Gd	11.6	8.8	13.8	14.9	21.9	22.4	10.6	6.1	10.0	*7.0*	*12.0*	*11.6*	*10.2*	*8.9*
Dy	13.3	11.0	14.4	14.1	23.6	24.2	9.4	7.3	10.0	*7.7*	*11.2*	*11.8*	*7.8*	*14.6*
Er	8.10	5.66	8.45	7.91	12.93	13.39	5.30	5.20	4.70	*3.70*	*8.10*	*7.40*	*4.40*	*4.90*
Yb	8.70	6.70	7.97	7.48	11.91	13.00	4.60	5.20	6.20	*3.60*	*7.80*	*6.70*	*2.50*	*5.50*
Lu	1.18	1.00	1.15	1.15	1.61	1.76	1.18	0.81	0.60	*0.27*	*0.99*	*0.59*	*0.37*	*0.51*
Hf	18.6	12.7	17.1	19.2	30.3	33.8	26.8	21.0	23.5	*6.9*	*12.8*	*14.5*	*9.2*	*13.2*
Ta	7.2	5.0	8.5	9.0	13.3	13.4	11.1	9.5	6.9	*3.2*	*6.8*	*6.1*	*4.5*	*6.9*
W	2.50	0.79	1.88	1.95	3.58	4.00	5.50	2.77	1.90	*0.54*	*2.00*	*1.03*	*1.00*	*1.14*
Pb	5.91	4.65	6.75	6.79	14.37	13.06	13.50	10.20	4.30	*2.90*	*4.10*	*6.30*	*3.50*	*6.20*
Th	10.9	7.8	10.8	10.7	21.1	21.8	20.5	16.0	16.0	*4.2*	*8.7*	*7.9*	*5.7*	*9.1*
U	3.15	2.02	3.33	3.40	6.42	6.32	7.00	5.80	5.70	*1.13*	*2.71*	*2.20*	*1.82*	*2.77*

Table 8: Intensive variables modelled for Ascension Island samples

Sample number	Region	FeTi-Oxide Thermometry[1]		Feldspar-melt Thermometry [2,3]	
		T (°C)	fO_2 (ΔNNO)	T (°C)	wt.% H_2O[4]
AI14-411	Youngest Sisters	935	-0.4	1150	
AI14-471	Older Sisters	--	--	1152	
AI14-423	Youngest Letterbox	990	-0.05	1093	
AI14-429	Older Letterbox	1025	+0.08	1110	
AI14-445	Youngest Wideawakes	985	-0.34	1167	
AI14-511	Cricket Valley	884	-1.6	886	5.2
AI14-428	White Horse	--	--	837	5.5
AI-94	Middleton's Ridge	--	--	772	4.7
AI-103	Mountain Red Hill	967	-1.9	801	7.2
AI14-419	Letterbox felsic lava	--	--	837	
AI15-621	Devil's Riding School	--	--	871	5.1
AI15-618	Youngest pumice fall	--	--	847	6.4
AI14-435A	Echo Canyon	--	--	993	
AI14-438	NE scoria	--	--	1164	
AI14-493A	NASA unit E	--	--	811	7.1
AI14-488A	NASA unit A	--	--	813	8.1
AI14-459A	Middleton's Valley fall	950	-0.2	1034	
AI14-552	Green Mountain scoria	--	--	1174	
AI14-439A[+]	*Compositionally-zoned scoria*	*845*	*-2.28*		
AI14-439G[+]	*Compositionally-zoned pumice*	*866*	*-1.94*		

[1]Using the calibration of Ghiorso & Evans, 2008, on oxides which have passed the equilibrium test of Bacon & Hirschmann (1988).

[2] Plagioclase-melt thermometry from Putirka (2008), only analyses where K_D(Ab-An) was 0.1 ± 0.11 for T < 1050 °C, or 0.27 ± 0.05 at T > 1050 °C were used (Putirka, 2008).

[3]Alkali-feldspar-melt thermometry (Putirka, 2008). Only analyses within the equilibrium bounds outlined in Mollo et al. (2015) were used.

[4] Alkali-feldspar-melt hygrometry (Mollo et al., 2015). Only analyses within the equilibrium bounds outlined in Mollo et al. (2015) were used. Uncertainties of ±0.7 wt.% consistent with that published in Mollo et al. (2015) are assumed.